Weather Prediction in SHiELD: Effect from GFDL Cloud Microphysics Scheme Upgrade

Linjiong Zhou[1], Lucas Harris[2], Jan-Huey Chen[3], Kun Gao[4], Huan Guo[5], Baoqiang Xiang[6], Mingjing Tong[5], J. Jacob Huff[7], and Matthew Morin[8]

[1]Geophysical Fluid Dynamics Laboratory
[2]GFDL
[3]NOAA GFDL/ UCAR
[4]Princeton University
[5]NOAA/GFDL
[6]NOAA/Geophysical Fluid Dynamics Laboratory, UCAR
[7]Woodwell Climate Research Center
[8]DRC/GFDL/NOAA

November 24, 2022

Abstract

This paper documents the third version of the GFDL cloud microphysics scheme (GFDL MP v3) used in the System for High-resolution prediction on Earth-to-Local Domains (SHiELD) model. Compared to the GFDL MP v2, the GFDL MP v3 is entirely reorganized, optimized, and modularized by functions. In addition, the particle size distribution (PSD) of all cloud categories is redefined to mimic the latest observations, and the cloud condensation nuclei (CCNs) are calculated from the MERRA2 aerosol data. The GFDL MP has been redesigned so all processes use the redefined PSD to ensure overall consistency and easily permit introductions of new PSDs and microphysical processes. Analyses gathered from simulations by SHiELD with selected configurations are examined. Compared to the GFDL MP v2, the GFDL MP v3 significantly improves the predictions of geopotential height, air temperature, and specific humidity in the Troposphere, as well as the high, middle and total cloud fractions and the liquid water path. With the more realistic PSD implemented in GFDL MP v3, the predictions of geopotential height in the Troposphere, low and total cloud fractions are further improved. Furthermore, using climatological aerosol data to calculate CCNs leads to even better predictions of geopotential height, air temperature, and specific humidity in the Troposphere, high and middle cloud fractions, as well as the liquid and ice water paths. However, the upgrade of the GFDL MP shows little impact on the precipitation prediction. Degradation due to the scheme upgrade is also addressed and discussed to guide the future GFDL MP development.

Weather Prediction in SHiELD: Effect from GFDL Cloud Microphysics Scheme Upgrade

Linjiong Zhou[1,2], Lucas Harris[2], Jan-Huey Chen[2,3], Kun Gao[1,2], Huan Guo[2], Baoqiang Xiang[2,3], Mingjing Tong[2], J. Jacob Huff[2,3], and Matthew Morin[2,3]

[1]Program in Atmospheric and Oceanic Sciences, Princeton University, Princeton, New Jersey, USA.
[2]National Oceanic and Atmospheric Administration / Geophysical Fluid Dynamics Laboratory, Princeton, New Jersey, USA.
[3]University Corporation for Atmospheric Research, Boulder, Colorado, USA.

Key Points:

- The GFDL cloud microphysics scheme has been re-written for greater physical consistency.
- The upgrade of the GFDL MP significantly improves weather prediction within the GFDL SHiELD model.
- The changes of PSD and CCNs in the GFDL MP show significant impacts on temperature, humidity, and cloud predictions.

Corresponding author: Linjiong Zhou, Linjiong.Zhou@noaa.gov

Abstract

This paper documents the third version of the GFDL cloud microphysics scheme (GFDL MP v3) used in the System for High-resolution prediction on Earth-to-Local Domains (SHiELD) model. Compared to the GFDL MP v2, the GFDL MP v3 is entirely reorganized, optimized, and modularized by functions. In addition, the particle size distribution (PSD) of all cloud categories is redefined to mimic the latest observations, and the cloud condensation nuclei (CCNs) are calculated from the MERRA2 aerosol data. The GFDL MP has been redesigned so all processes use the redefined PSD to ensure overall consistency and easily permit introductions of new PSDs and microphysical processes.

Analyses gathered from simulations by SHiELD with selected configurations are examined. Compared to the GFDL MP v2, the GFDL MP v3 significantly improves the predictions of geopotential height, air temperature, and specific humidity in the Troposphere, as well as the high, middle and total cloud fractions and the liquid water path. With the more realistic PSD implemented in GFDL MP v3, the predictions of geopotential height in the Troposphere, low and total cloud fractions are further improved. Furthermore, using climatological aerosol data to calculate CCNs leads to even better predictions of geopotential height, air temperature, and specific humidity in the Troposphere, high and middle cloud fractions, as well as the liquid and ice water paths. However, the upgrade of the GFDL MP shows little impact on the precipitation prediction. Degradation due to the scheme upgrade is also addressed and discussed to guide the future GFDL MP development.

Plain Language Summary

The Geophysical Fluid Dynamics Laboratory (GFDL) cloud microphysics (MP) scheme has been recently upgraded to improve the code's structure and flexibility, and overall consistency, include more realistic cloud particle size distribution (PSD), and use the climatological aerosol to calculate cloud condensation nuclei (CCNs). The primary purpose of the GFDL MP upgrade is to improve global weather prediction, which includes geopotential height, temperature, specific humidity, cloud, and precipitation predictions. The implementation of the upgraded GFDL MP significantly improves the weather prediction of many key fields. Especially, the use of the more realistic cloud PSD and climatological aerosol for CCNs can further improve the prediction skill of the model to some extent.

1 Introduction

Clouds play critical roles in our daily weather and in the global energy and water budgets that regulate the climate of the Earth (Houze, 2014; Lamb & Verlinde, 2011). The formation and evolution of clouds have significant impacts on precipitation forecasts in numerical weather prediction (Baldauf et al., 2011; Bauer et al., 2015; Morrison & Grabowski, 2008; Seifert & Beheng, 2005). Clouds and their impacts on solar and thermal radiation are among the most challenging aspects of climate prediction (Stephens et al., 2012; Trenberth et al., 2009; Wild et al., 2019). Therefore, the representation of clouds in atmospheric models deserves particular attention. Since numerical models ranging from large-eddy simulations to climate predictions still cannot depict the cloud processes explicitly, the parameterization of cloud microphysics is needed (Kogan, 2013; Morrison & Gettelman, 2008; Nogherotto et al., 2016).

The national operational forecast system, Global Forecast System (GFS) at the National Centers for Environmental Prediction (NCEP), used the prognostic cloud microphysics scheme developed by Zhao and Carr (1997) from 1995 to 2019. Different from the simple large-scale saturation adjustment scheme (Hoke et al., 1989) used in the early versions of GFS, this prognostic cloud microphysics scheme explicitly calculates the combined cloud water and cloud ice category in the large-scale condensation component of the model (Zhao et al., 1997). The cloud water/ice mass mixing ratio is the only variable predicted in the Zhao and Carr (1997) scheme for both cloud water and cloud ice. This treatment saves the model computational time and storage and has been used exclusively since 1995. According to Zhao et al. (1997), forecasts using the Zhao and Carr (1997) scheme improved the forecast skill of precipitation as measured by the equitable threat score and bias score and reduced root-mean-square errors of forecast specific humidity at all pressure levels below 800 hPa and above 500 hPa during test periods over those of forecasts that only used diagnostic clouds.

There is an apparent deficiency in the Zhao and Carr (1997) scheme. The oversimplified treatment of cloud water and cloud ice inevitably excludes the interaction between cloud water and cloud ice, such as freezing and melting. As computational resources rapidly expand in recent decades, more sophisticated cloud microphysics schemes have been developed and used in weather and climate models. For example, the European Centre for Medium-Range Weather Forecasts replaced the ancient Tiedtke (1993) scheme with the advanced Forbes and Tompkins (2011); Forbes et al. (2011) prognostic scheme for the Integrated Forecast System in 2010. The National Center for Atmospheric Research upgraded the Rasch and Kristjánsson (1998) prognostic condensate and precipitation scheme to the well-known Morrison and Gettelman (2008) scheme for the Community Atmosphere Model version 5 in 2012. Much research has shown that by using a more comprehensive cloud microphysics scheme, one can achieve better weather prediction and climate simulation (Khain et al. (2015); Guo et al. (2021) and references therein). After extensive examinations with comprehensive verification, NCEP chose to replace the Zhao and Carr (1997) cloud microphysics scheme with the Geophysical Fluid Dynamics Laboratory (GFDL) cloud microphysics (MP) scheme (J. H. Chen & Lin, 2013; Zhou et al., 2019) in the GFS upgrade of June 2019, aiming to better represent the interaction between each cloud category to improve weather prediction.

The GFDL MP is a six-category, single-moment bulk microphysics scheme. Besides the water vapor category, there are two liquid categories (cloud water and rain) and three ice categories (cloud ice, snow, and graupel or hail). Zhou et al. (2019) and L. Harris, Zhou, Lin, et al. (2020) have described key features of the GFDL cloud microphysics scheme, including thermodynamic consistency with the dynamical core, fast and stable sedimentation processes, and tight coupling between dynamics and physics. The GFDL cloud microphysics scheme has been used as the default scheme in the operational GFS version 15 and 16 (Tong et al., 2020; Huang et al., 2021; Patel et al., 2021) and several other weather and climate models, including the GFDL radiative-convective equilibrium (RCE) simulations within a limited domain (Jeevanjee, 2017), the GFDL High-resolution Atmosphere Model (HiRAM) (J. H. Chen & Lin, 2011, 2013; L. M. Harris et al., 2016; Gao et al., 2017, 2019), the GFDL System for High-resolution prediction on Earth-to-Local Domains (SHiELD) (L. Harris, Zhou, Lin, et al., 2020), the National Oceanic and Atmospheric Administration's Hurricane Analysis and Forecast System (HAFS) (Dong et al., 2020; A. Hazelton et al., 2021), the Chinese Academy of Sciences Flexible Global Ocean-Atmosphere-Land System Model (Zhou et al., 2015; Li et al., 2019; He et al., 2019), and the National Aeronautics and Space Administration Goddard Earth Observing System (GEOS) version 5 (Arnold et al., 2020).

Notably, the GFDL cloud microphysics scheme is now mainly developed within SHiELD at GFDL. Although the performance of SHiELD has gradually improved over the years with the continuous upgrades of the GFDL MP, cloud, precipitation, and radiation predictions are still challenging. For example, ice cloud fraction is under-predicted and so the long-wave radiation at the top of the atmosphere is significantly over-estimated. Liquid cloud fraction is also largely under-predicted over the global ocean area. SHiELD tends to predict excessive light and extreme precipitation and under-predict medium precipitation according to the analyses in L. Harris, Zhou, Lin, et al. (2020). The variable-resolution SHiELD with the GFDL MP is still struggling in predicting the strength and location of the convective-scale precipitation over the contiguous United States (Zhou et al., 2019). Leighton et al. (2020) pointed out that an unrealistic representation of the particle size distribution of cloud condensates in cloud microphysics schemes leads to the limited representation of the cloud variability and degradation of tropical cyclone prediction. Fan et al. (2016) pointed out that aerosol-cloud interaction is essential and has significant impacts on radiative forcing, precipitation, extreme weather, and large-scale circulation in their review paper.

This paper aims to document the most recent upgrade of the GFDL cloud microphysics scheme and understand the impacts of the more realistic particle size distribution and the use of climatological aerosol for cloud condensation nuclei on the global temperature, humidity, cloud, and precipitation predictions, and serves as a reference for future development. This paper is organized as follows. Section 2 briefly introduces the model used in this study. Section 3 documents the upgrade of the GFDL cloud microphysics scheme in detail. Section 4 presents the upgraded GFDL MP's impacts on weather prediction via detailed verification. Section 5 demonstrates the effects of the realistic particle size distribution and the use of climatological aerosol for cloud condensation nuclei on weather prediction. Finally, we end up with a summary and discussion in section 6.

2 Model Description

The model used in this study is the System for High-resolution prediction on Earth-to-Local Domains (SHiELD). SHiELD, previously called fvGFS (finite-volume Global Forecast System) (A. T. Hazelton et al., 2018; Zhou et al., 2019; J. Chen et al., 2019; J. H. Chen et al., 2019), was developed as a prototype of the Next-Generation Global Prediction System of the National Weather Service and the broader Unified Forecast System (UFS) (L. Harris, Zhou, Lin, et al., 2020). SHiELD can be used for applications on a broad range of time scales but has been designed with a particular focus on weather (up to 10 days) (L. M. Harris et al., 2019) and subseasonal-to-seasonal (S2S; between two weeks and one season) (L. Harris, Zhou, Lin, et al., 2020) predictions. Notably, advances in SHiELD have migrated into UFS models slated for operational implementations at NCEP, including the GFS version 15 and version 16.

In this study, all SHiELD simulations use the non-hydrostatic solver within the Finite-Volume Cubed-Sphere Dynamical Core (FV3) developed at GFDL (L. M. Harris & Lin, 2013; S.-J. Lin, 2004; Putman & Lin, 2007; L. Harris, Zhou, Chen, & Chen, 2020; L. Harris, Chen, et al., 2020). The physical parameterization suite in SHiELD originated from that in GFS version 14 (J. Chen et al., 2019), but contains substantial updates in the following processes: the microphysics scheme of Zhao and Carr (1997) and cloud fraction scheme of Xu and Randall (1996) are replaced by the inline GFDL cloud microphysics parameterizations (Zhou et al., 2019; L. Harris, Zhou, Lin, et al., 2020). The cloud-radiation interaction was redesigned to combine the cloud microphysics processes and cloud radiative properties. To incorporate atmosphere-ocean interaction, we have implemented a mixed layer ocean module based on Pollard et al. (1973). This simple ocean model computes the mixed layer depth and temperature within that mixed layer as prognostic variables, driven by surface wind stress and heat fluxes from the atmosphere together with a nudging toward climatology applied to the mixed layer temperature and mixed-layer depth (L. Harris, Zhou, Lin, et al., 2020). In the latest version of SHiELD that is used in this paper, the convection schemes (J. G. Han et al., 2017), planetary boundary layer scheme (J. Han & Bretherton, 2019), and land surface model (Ek et al., 2003) are all updated to synchronize the current operational GFS version 16.

3 Cloud Microphysics Parameterization

The first version of the GFDL cloud microphysics scheme (GFDL MP v1, Zhou et al. (2019)) originated from J. H. Chen and Lin (2013), was mainly developed for fvGFS to support the upgrade of operational GFS version 15. It was a split cloud microphysics scheme in which the saturation adjustment processes were built inside the FV3 dynamical core. This version, with some minor upgrades, is still in use in the operational GFS version 16. Later the second version of the GFDL cloud microphysics scheme (GFDL MP v2, L. Harris, Zhou, Lin, et al. (2020)) was developed entirely inside the FV3 dynamical core in SHiELD. We call this the "inline GFDL MP". Recently, the GFDL MP in SHiELD has been dramatically updated. We call this the third version of the GFDL MP as it is significantly different from the second version. Compared with the GFDL MP v2, the code of the GFDL MP v3 is entirely reorganized, optimized, and modularized by functions for the first time. All scientific updates are described in Appendix A. The improvements from the GFDL MP v3 in weather prediction are demonstrated in the following sections.

Among all the updates in the GFDL MP v3, the update of particle size distribution and the overall consistency are essential and significant. First, the particle size distributions for all six cloud categories are redefined as a gamma distribution to mimic the latest observations. As a result, the cloud water and cloud ice are no longer mono-dispersed as in the GFDL MP v2. The large cloud categories, e.g., rain, snow, and graupel, or hail, still follow the exponential distribution as suggested by most observations and literature (Khain et al. (2015) and references therein), and which is a special case of the gamma distribution. Along with the particle size distribution upgrade, microphysical processes, e.g., accretion, evaporation, sublimation/deposition, and freezing/melting, have been reformatted and overhauled accordingly. This ensures an overall microphysical consistency and easily permits introductions of new particle size distributions, microphysical processes, and multi-moment distributions. Details of these updates are described in the following subsections. Due to the introduction of the more realistic particle size distribution and reformation of many microphysical processes, the computational runtime of the microphysics scheme increases by about 20%, but it is negligible (about 2%) compared to the total model runtime in SHiELD.

3.1 Particle Size Distribution

The particle size distribution (PSD) describes the microstructure of a cloud category in each grid box. By definition, the concentration of a cloud particle is a function of the particle size. In general, the PSD functions can be mono-dispersed, exponential, gamma, or log-normal distribution. These distributions are normalizable and integratable over complete size distributions of diameter from zero to infinity, or partial distributions from diameter of zero to D_1 or D_2 to infinity or even D_1 to D_2 (Straka, 2009). All cloud properties and cloud processes can then be parameterized based on the PSD functions. In the GFDL MP v3, the PSD of each cloud category is parameterized with gamma distribution containing three parameters:

$$n\left(D\right) = n_0 D^{\mu-1} \exp\left(-\lambda D\right), \tag{1}$$

where n_0 (unit: $m^{-3-\mu}$) is called the intercept parameter, μ (unit: 1) is called the spectral shape parameter, λ (unit: m^{-1}) is called the slope parameter, and D (unit: m) is the particle's diameter. When the spectral shape parameter μ equals to 1, it becomes an exponential distribution. In a single-moment bulk cloud microphysics scheme with prognostic mass mixing ratio q (unit: $kg\ kg^{-1}$), the intercept parameter n_0 and spectra shape parameter μ are predefined, while the slope parameter λ can be derived from n_0, μ, and q. The values of n_0 and μ for each cloud category of the GFDL MP v3 are listed in Table 1. Those parameters for cloud water, cloud ice, rain, snow, and graupel or hail are derived based on Martin et al. (1994), Fu (1996), Marshall and Palmer (1948),

Table 1. The intercept parameter (n_0, unit: $m^{-3-\mu}$), spectral shape parameter (μ, unit: 1), density of cloud category (ρ_0, unit: $kg\ m^{-3}$), parameter α (unit: $m^{1-\beta}\ s^{-1}$) and β for each cloud category of the GFDL MP v3.

	Cloud Water	Cloud Ice	Rain	Snow	Graupel	Hail
n_0	1.2×10^{66}	1.0×10^{10}	8×10^6	3×10^6	4×10^6	4×10^4
μ	11	1	1	1	1	1
ρ_0	1×10^3	9.17×10^2	1×10^3	1×10^2	4×10^2	9.17×10^2
α	3×10^7	11.72	842	4.8	1	1
β	2	0.41	0.8	0.25	0.5	0.5

Gunn and Marshall (1958), and Houze et al. (1979) or Federer and Waldvogel (1975), respectively.

The particle size distribution (PSD) is not simply a function of diameter (D), as shown in Equation (1). It also depends on cloud content (ρq) or the mass mixing ratio of cloud (q) because the slope parameter (λ, defined below) is a function of q. Figure 1 shows that cloud water droplet number follows gamma distribution while all other cloud categories follow exponential distribution at a specified cloud content. The particle number of cloud categories increases when cloud content increases. As shown in Figure 1a,b, most cloud water droplets have sizes between 6 μm and 40 μm, with a peak particle number at around 20 μm. Cloud water droplet number is three orders of magnitude less when the cloud water content drops from 10 $g\ m^{-3}$ to 10^{-4} $g\ m^{-3}$. Different from cloud water, cloud ice particle number monotonically decreases as particle size increases (Figure 1c,d). As shown in Figure 1e-l, the distributions of rain, snow, graupel, and hail particle numbers are similar, except that rain has the highest particle number while hail has the lowest particle number because rain (hail) has the highest (lowest) intercept parameter (n_0). Rain, snow, graupel, and hail particle sizes approach zero at radii between 2000 μm to 6000 μm, depending on the particular species and the water content. Higher water content is needed to produce non-negligible numbers of the largest particles. In the GFDL MP v3, cloud ice particle number still follows the exponential distribution as Fu (1996). The same PSD assumption is applied to the calculation of cloud ice radiative property. Recent studies, e.g., McFarquhar et al. (2015), used new observations to show cloud ice should follow the gamma distribution. As the PSD of cloud ice is written in gamma distribution format, we can change its PSD in the future.

3.2 Quantities Characterizing Cloud Parameters

Once the PSD is defined, we can derive the particle concentration (N, unit: m^{-3}), effective diameter (D_{eff}, unit: m), optical extinction (β, unit: m^{-1}), mass mixing ratio (q, unit: $kg\ kg^{-1}$), and radar reflectivity factor (Z, unit: m^3) by integrating the PSD over all diameters:

$$N = \int_0^\infty n(D)\,dD = \frac{n_0 \Gamma(\mu)}{\lambda^\mu}, \tag{2}$$

$$D_{\text{eff}} = \frac{\int_0^\infty D^3 n(D)\,dD}{\int_0^\infty D^2 n(D)\,dD} = \frac{\mu+2}{\lambda}, \tag{3}$$

$$\beta = \frac{\pi}{2}\int_0^\infty D^2 n(D)\,dD = \frac{\pi n_0 \Gamma(\mu+2)}{2\lambda^{\mu+2}}, \tag{4}$$

$$q = \frac{\pi}{6}\frac{\rho_0}{\rho}\int_0^\infty D^3 n(D)\,dD = \frac{\pi \rho_0 n_0 \Gamma(\mu+3)}{6\rho\lambda^{\mu+3}}, \tag{5}$$

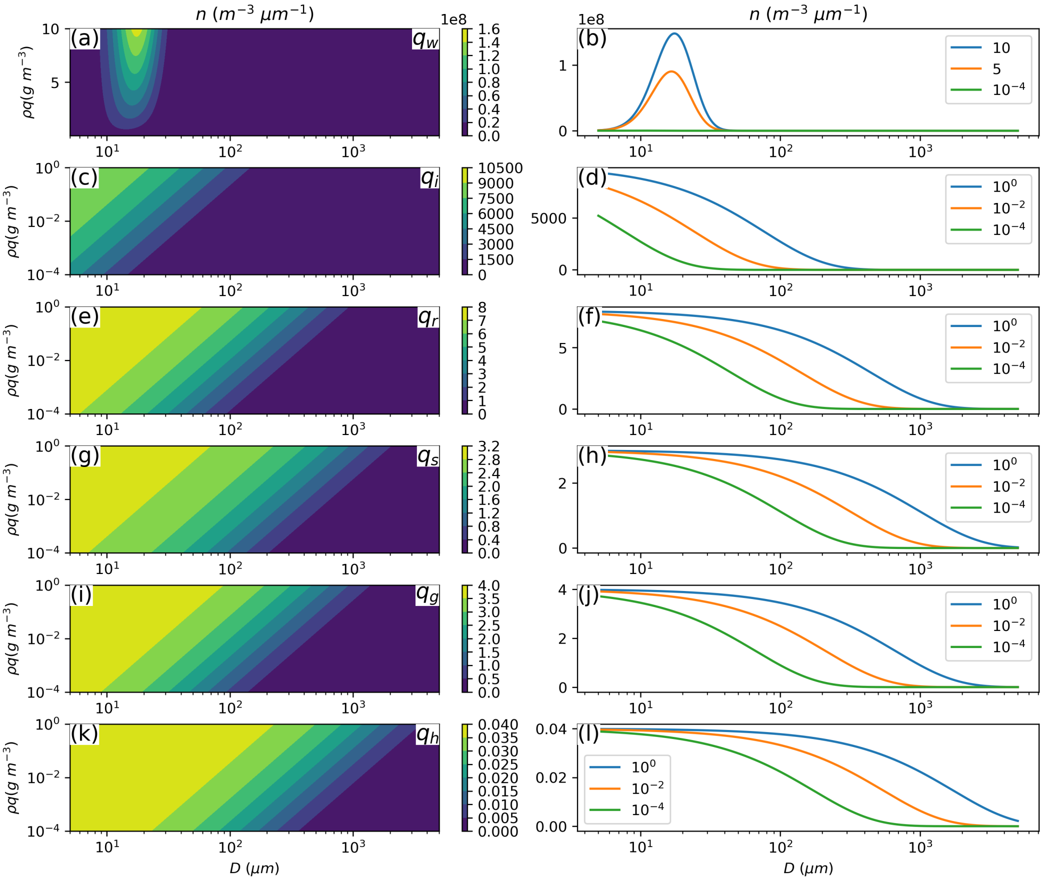

Figure 1. (a, c, e, g, i, k) Particle size distribution (PSD, n, unit: m^{-3} μm^{-1}) as a function of diameter (D, unit: μm) and cloud content (ρq, unit: g m^{-3}). (b, d, f, h, j, l) PSD as a function of diameter at three selected cloud water content amounts. (a) and (b) are cloud water (q_w), (c) and (d) are cloud ice (q_i), (e) and (f) are rain (q_r), (g) and (h) are snow (q_s), (i) and (j) are graupel (q_g), and (k) and (l) are hail (q_h).

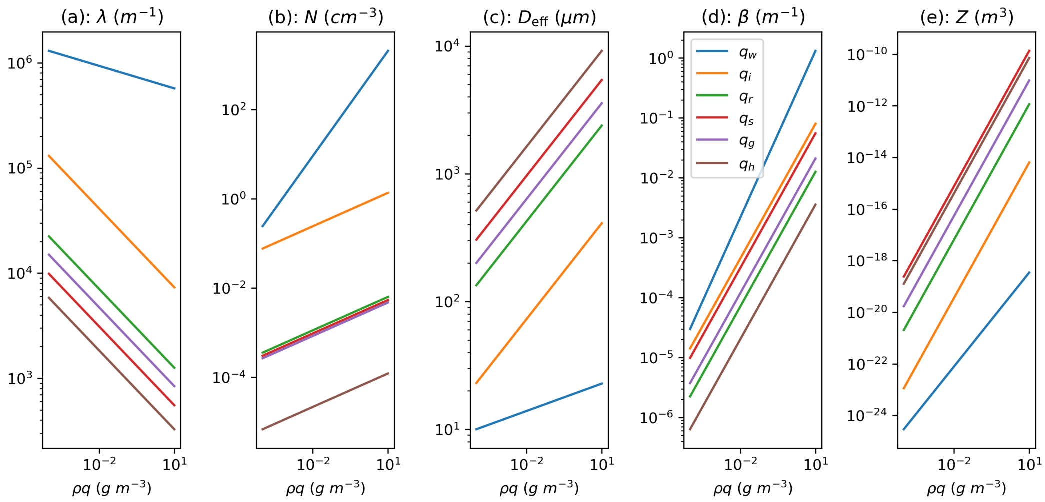

Figure 2. From left to right are the the (a) slope parameter (λ, unit: m^{-1}), (b) particle concentration (N, unit: cm^{-3}), (c) effective diameter (D_{eff}, unit: μm), (d) optical extinction (β, unit: m^{-1}), and (e) radar reflectivity factor (Z, unit: m^3) for each cloud category as a function of cloud content (ρq, unit: $g\ m^{-3}$). Blue, orange, green, red, purple, and brown lines are the quantities of cloud water (q_w), cloud ice (q_i), rain (q_r), snow (q_s), graupel (q_g), and hail (q_h).

$$Z = \int_0^\infty D^6 n\,(D)\,dD = \frac{n_0 \Gamma\,(\mu+6)}{\lambda^{\mu+6}}. \tag{6}$$

The density (ρ_0) of each cloud category is listed in Table 1. ρ is the density of air. In the single-moment case where the mass mixing ratio (q) is a prognostic variable, the slope parameter (λ) can be derived from Equation (5):

$$\lambda = \left[\frac{\pi \rho_0 n_0 \Gamma\,(\mu+3)}{6\rho q}\right]^{1/(\mu+3)}. \tag{7}$$

By definition, and apparent from Figure 2, the slope parameter (λ), particle concentration (N), effective diameter (D_{eff}), optical extinction (β), and radar reflectivity factor (Z) are all a power function of cloud content (ρq). As shown in Figure 2b, assuming the same cloud content, the particle concentration of cloud water is an order of magnitude larger than cloud ice and two orders of magnitude larger than rain, snow, and graupel. Hail is an order of magnitude less than graupel. The increment of cloud water particle concentration regarding cloud water content is about two orders larger than other cloud categories. As shown in Figure 2c, the effective diameter of cloud water is about 10 μm to 20 μm, and cloud ice is about 20 μm to 400 μm. The effective diameters of rain, graupel, snow, and hail are close, with the latter larger than the former. As shown in Figure 2d, the optical extinction of all cloud categories is quite close and similar to each other in tendency. Optical extinction is the largest for cloud water and the smallest for hail, with two orders of difference. As shown in Figure 2e, cloud water has the smallest radar reflectivity factor, but snow and hail have the largest.

We briefly describe how this method can be easily extended to a double-moment (DM) scheme, in which both the particle concentration (N) and mass mixing ratio (q) are prognostic variables. The intercept parameter (n_0^{DM}) and slope parameter (λ^{DM}) can be derived from the combination of Equation (2) and (5):

$$n_0^{DM} = \frac{N^{1+\mu/3}}{\Gamma\,(\mu)}\left[\frac{\pi \rho_0 \Gamma\,(\mu+3)}{6\rho q \Gamma\,(\mu)}\right]^{\mu/3}, \tag{8}$$

$$\lambda^{DM} = \left[\frac{\pi\rho_0 N\Gamma(\mu+3)}{6\rho q\Gamma(\mu)}\right]^{1/3}. \tag{9}$$

In this case, the spectra shape parameter (μ) is the only variable that needs to be predefined or parameterized. For cloud water, following Morrison and Gettelman (2008), it is defined as:

$$\mu^{DM} = \frac{1}{(0.000571N_c + 0.2714)^2}. \tag{10}$$

Where N_c (unit: cm^{-3}) is the cloud droplet number concentration defined separately in different cloud scenario. When N_c equals to 52.827 cm^{-3}, μ^{DM} is 11, the one that used in the current single-moment scheme. For cloud ice, following Morrison and Milbrandt (2015), it is defined as:

$$\mu^{DM} = 0.00191\left(\lambda^{DM}\right)^{0.8} - 2. \tag{11}$$

For all other cloud categories, $\mu^{DM} = 1$. The double-moment extension of the GFDL MP is still under development and is not used in this paper. However as shown here the double-moment scheme can be implemented as an extension of the current single-moment scheme, and serves as a reference for future GFDL MP development.

3.3 Terminal Velocity

Terminal velocity (V) is generally given as a power-law relationship with respect to particle size (Straka, 2009):

$$V = \alpha D^{\beta}, \tag{12}$$

The leading coefficient α and the power β for each cloud categories are listed in Table 1. The parameters for cloud water, cloud ice, rain, snow, and graupel or hail follow Ikawa and Saito (1991), McFarquhar et al. (2015), Liu and Orville (1969), Straka (2009), and Pruppacher and Klett (2010), respectively. The terminal velocity used in the microphysical processes can be weighted by number (V_N), mass (V_M), or even reflectivity (V_Z) corresponding to each moment (Milbrandt & Yau, 2005). After applying the gamma distribution, the terminal velocities can be written as:

$$V_N = \frac{\int_0^\infty Vn(D)\,dD}{\int_0^\infty n(D)\,dD} = \frac{\alpha\Gamma(\mu+\beta)}{\lambda^\beta\Gamma(\mu)}, \tag{13}$$

$$V_M = \frac{\int_0^\infty VD^3n(D)\,dD}{\int_0^\infty D^3n(D)\,dD} = \frac{\alpha\Gamma(\mu+\beta+3)}{\lambda^\beta\Gamma(\mu+3)}, \tag{14}$$

$$V_Z = \frac{\int_0^\infty VD^6n(D)\,dD}{\int_0^\infty D^6n(D)\,dD} = \frac{\alpha\Gamma(\mu+\beta+6)}{\lambda^\beta\Gamma(\mu+6)}. \tag{15}$$

Generally, the reflectivity weighted terminal velocity (V_Z) is larger than the mass weighted terminal velocity (V_M), which is further larger than the number weighted terminal velocity (V_N) (Milbrandt & Yau, 2005). It can also be seen in Figure 3, the terminal velocity of cloud water is the smallest (≈ 0.01 $m\ s^{-1}$), followed by cloud ice (≈ 0.1–0.7 $m\ s^{-1}$), snow ($\approx 0.5-2$ $m\ s^{-1}$), graupel ($\approx 0.4-4$ $m\ s^{-1}$), rain ($\approx 0.4-10$ $m\ s^{-1}$), and hail (≈ 0.7–20 $m\ s^{-1}$). In the GFDL MP, the mass-weighted terminal velocity is used following Y. L. Lin et al. (1983), because the mass mixing ratio is the only prognostic moment. Note that unlike most microphysical schemes, including earlier versions of the GFDL MP, the GFDL MP v3 includes sedimentation of cloud water.

3.4 Microphysical Processes

Since the PSDs are redefined, many cloud microphysical processes are reformulated accordingly to ensure an overall microphysical consistency and easily permit introductions of new particle size distributions, microphysical processes, and multi-moment distributions. Those cloud microphysical processes include accretion, evaporation, sublimation, deposition, melting, and freezing derived initially based on the PSD.

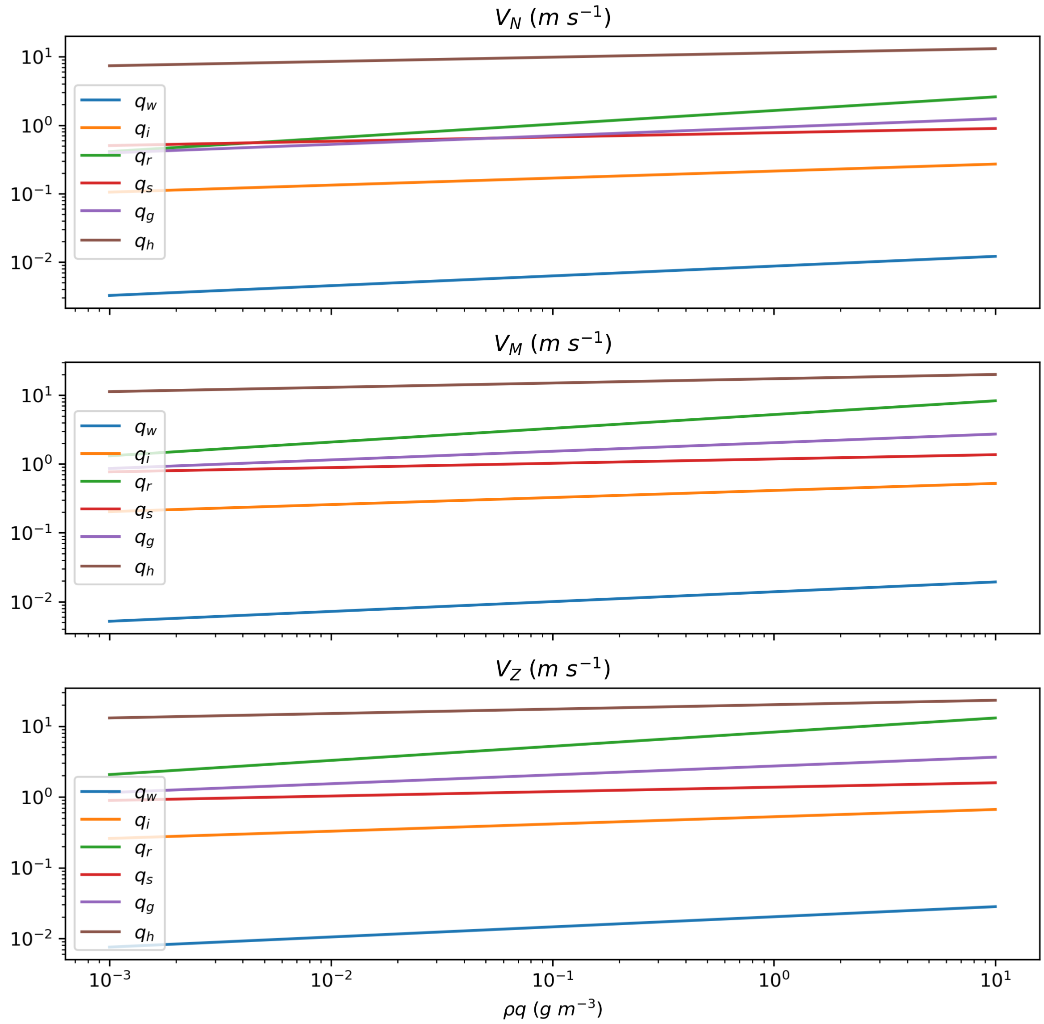

Figure 3. From top to bottom are the number weighted (V_N), mass weighted (V_M), and reflectivity weighted (V_Z) terminal velocities (unit: $m\ s^{-1}$) as a function of water content (ρq, unit: $g\ m^{-3}$). Blue, orange, green, red, purple, and brown lines are the terminal velocities of cloud water (q_w), cloud ice (q_i), rain (q_r), snow (q_s), graupel (q_g), and hail (q_h).

Accretion between each two falling cloud categories follows Wisner et al. (1972). The accretion rate between cloud x and y (P_{xacy}, accretion of y by x, unit: $kg\ kg^{-1}\ s^{-1}$) is reformulated after putting the gamma distribution in and integrating the particle size from zero to infinity:

$$P_{xacy} = \int_0^\infty \int_0^\infty \frac{\pi^2}{24} E_{xy} \left| V_x - V_y \right| \frac{\rho_{y0}}{\rho} \left(D_x + D_y \right)^2 D_y^3 n_x \left(D_x \right) n_y \left(D_y \right) dD_x dD_y$$

$$= \frac{\pi^2}{24} E_{xy} n_{x0} n_{y0} \left| V_x - V_y \right| \frac{\rho_{y0}}{\rho} \left[\frac{\Gamma\left(\mu_x\right)\Gamma\left(\mu_y+5\right)}{\lambda_x^{\mu_x}\lambda_y^{\mu_y+5}} + \frac{\Gamma\left(\mu_x+2\right)\Gamma\left(\mu_y+3\right)}{\lambda_x^{\mu_x+2}\lambda_y^{\mu_y+3}} + \frac{2\Gamma\left(\mu_x+1\right)\Gamma\left(\mu_y+4\right)}{\lambda_x^{\mu_x+1}\lambda_y^{\mu_y+4}} \right], \quad (16)$$

where V_x and V_y are the terminal velocities of cloud x and y, respectively. E_{xy} is the collection efficiency between cloud x and y. Specifically, $E_{rw} = 0.35$, $E_{ri} = 1.0$, $E_{sw} = 1.0$, $E_{si} = 0.35$, $E_{sr} = 1.0$, $E_{gw}/E_{hw} = 1 \times 10^{-4}$, $E_{gi}/E_{hi} = 0.05$, $E_{gr}/E_{hr} = 1.0$, and $E_{gs}/E_{hs} = 0.01$. This formula can be simplified when one of the two cloud categories (e.g., y) does not fall and is distributed mono-dispersedly as:

$$P_{xacy} = \int_0^\infty \frac{\pi}{4} E_{xy} q_y V_x D_x^2 n_x \left(D_x \right) dD_x = \frac{\pi E_{xy} n_{x0} \alpha_x q_y \Gamma\left(\mu_x + \beta_x + 2\right)}{4\lambda^{\mu_x+\beta_x+2}}, \quad (17)$$

The exponential case ($\mu = 1$) of Equation (16) and (17) are widely used in the Y. L. Lin et al. (1983) scheme and in early versions of the GFDL MP scheme.

Evaporation, sublimation and deposition follow Byers (1965). The evaporation / sublimation / deposition rate (P_{ESD}, unit: $kg\ kg^{-1}\ s^{-1}$) is reformulated after putting the gamma distribution in and integrating the particle size from zero to infinity:

$$P_{ESD} = \int_0^\infty \frac{2\pi\left(S-1\right)}{\rho\left(A+B\right)} V_f D n\left(D\right) dD = \frac{2\pi\left(S-1\right)}{\rho\left(A+B\right)} \frac{n_0 \Gamma\left(\mu+1\right)}{\lambda^{\mu+1}} V_f, \quad (18)$$

where S is the ratio between saturated mixing ratio of water vapor (q_{sat}) and water vapor mixing ratio (q_v), A and B are thermodynamics terms defined as:

$$A = \frac{L^2}{K_a R_v T^2}, \quad (19)$$

$$B = \frac{1}{\rho q_{sat} \psi}, \quad (20)$$

where L is the latent heat coefficient, $K_a = 2.36 \times 10^{-2}\ J\ m^{-1}\ s^{-1}\ K^{-1}$ is the thermal conductivity of air, R_v is gas constant of water vapor, T is air temperature, and $\psi = 2.11 \times 10^{-5}\ m^2\ s^{-1}$ is diffusivity of water vapor.

The ventilation coefficient (V_f) in Equation (18) is defined followed Beard and Pruppacher (1971). After putting the gamma distribution in and integrating the particle size from zero to infinity, V_f is reformatted as:

$$V_f = 0.78 + 0.31 S_c^{1/3} \nu^{-1/2} \frac{\int_0^\infty V^{1/2} D^{3/2} n\left(D\right) dD}{\int_0^\infty D n\left(D\right) dD} = 0.78 + 0.31 S_c^{1/3} \nu^{-1/2} \frac{\alpha^{1/2} \Gamma\left(\mu + \frac{\beta+3}{2}\right)}{\lambda^{\mu+\frac{\beta+3}{2}}} \frac{\lambda^{\mu+1}}{\Gamma\left(\mu+1\right)}, \quad (21)$$

where $\nu = 1.259 \times 10^{-5}\ m^2\ s^{-1}$ is the kinematic viscosity of air and $S_c = \nu/\psi$ is the Schmidt number.

The melting process follows Mason (1971). The melting rate (P_{melt}, unit: $kg\ kg^{-1}\ s^{-1}$) is reformulated after putting the gamma distribution in and integrating the particle size from zero to infinity:

$$P_{melt} = \int_0^\infty \frac{2\pi}{\rho L} \left[K_a \left(T - T_0\right) - L\psi\rho\left(q_{sat} - q_v\right) \right] V_f D n\left(D\right) dD$$

$$= \frac{2\pi}{\rho L} \left[K_a \left(T - T_0\right) - L\psi\rho\left(q_{sat} - q_v\right) \right] \frac{n_0 \Gamma\left(\mu+1\right)}{\lambda^{\mu+1}} V_f, \quad (22)$$

where T_0 is the freezing temperature.

At last, the rain freezing process follows Wisner et al. (1972). The freezing rate (P_{fr}, unit: $kg\ kg^{-1}\ s^{-1}$) is reformulated after putting the gamma distribution in and integrating the particle size from zero to infinity:

$$\begin{aligned} P_{fr} &= \int_0^\infty \frac{\pi^2}{36} D^6 \frac{\rho_0}{\rho} B' \exp\left[A'\left(T_0 - T\right) - 1\right] n\left(D\right) dD \\ &= \frac{\pi^2}{36} n_0 \frac{\rho_0}{\rho} B' \exp\left[A'\left(T_0 - T\right) - 1\right] \frac{\Gamma\left(\mu + 6\right)}{\lambda^{\mu+6}}, \end{aligned} \tag{23}$$

where $A' = 0.66\ K^{-1}$ and $B' = 100\ m^{-3}\ s^{-1}$ are two constant parameters following Bigg (1953).

The following microphysical processes remain the same from GFDL MP v2: 1) condensation and evaporation of cloud water, 2) deposition and sublimation of cloud ice, 3) cloud ice freezing and melting, 3) cloud water autoconversion, 5) cloud ice aggregation or autoconversion, 6) snow aggregation or autoconversion. Future GFDL MP development will include the particle size distribution to these remaining processes.

3.5 Cloud Condensation Nuclei

Among these microphysical processes, cloud water to rain autoconversion follows the equation (15) in Rotstayn (1997). In this process, the cloud droplet concentration is a key factor. The cloud droplet concentration in the current version of GFDL MP is an input parameter which is parameterized as a function of cloud condensation nuclei (CCNs). According to equation (15) in Rotstayn (1997), the more CCNs in the cloud, the slower is the cloud water to rain autoconversion. For simplicity, the CCNs in the GFDL MP v2 used two fixed values over the land and the ocean, respectively. The land value of 300 cm^{-3} is from Tripoli and Cotton (1980), while the ocean value of 100 cm^{-3} is from Rotstayn (1997). Therefore, the aerosol-related microphysical processes and the aerosol-cloud interactions may not be properly represented in the GFDL MP v2 due to unrealistic CCNs distribution.

In the GFDL MP v3 we instead use aerosol data in the Modern-Era Retrospective analysis for Research and Applications, version 2 (MERRA2) (Rienecker et al., 2011) from the National Aeronautics and Space Administration (NASA) Goddard Earth Science Data Information and Services Center (GES DISC). This aerosol product is one of the reanalyses from the Goddard Earth Observing System Model, Version 5 (GEOS-5) data assimilation system (Randles et al., 2017; Gelaro et al., 2017). We combined the 3-hourly aerosol data from 2015 to 2020 to create a 12-month climatological dataset consisting of 72 vertical levels from the surface to about 1.3 Pa at the top. The horizontal resolution is 0.5 by 0.625 degrees. The species of sulfate, which is a subset of MERRA2 aerosol, is converted to CCNs using Boucher and Lohmann (1995) formula before feeding in the GFDL MP v3.

Figures 4a,b show the geographic distribution of surface climatological CCNs derived from MERRA2 and its difference from the values used in the GFDL MP v2 (300 and 100 cm^{-3} over the land and the ocean, respectively). Over most of the land area except southeastern China and northern India, the CCNs from MERRA2 is below 300 cm^{-3}. The CCNs over all of Antarctica is below 100 cm^{-3}. Over most of the ocean area except the offshore of Asia and Europe, the east coast of North America, and the northern Pacific Ocean, the CCNs from MERRA2 is below 100 cm^{-3}. Only the CCNs over the offshore of China and India can reach to above 300 cm^{-3}. This comparison indicates that the fixed values of CCNs used in the GFDL MP v2 are substantially overestimated over most of the global area. Besides the horizontal spatial variability, the CCNs from MERRA2 also has vertical variability. Figure 4c shows that the vertical mean distributions and ranges decrease with height and are much smaller than the fixed values used

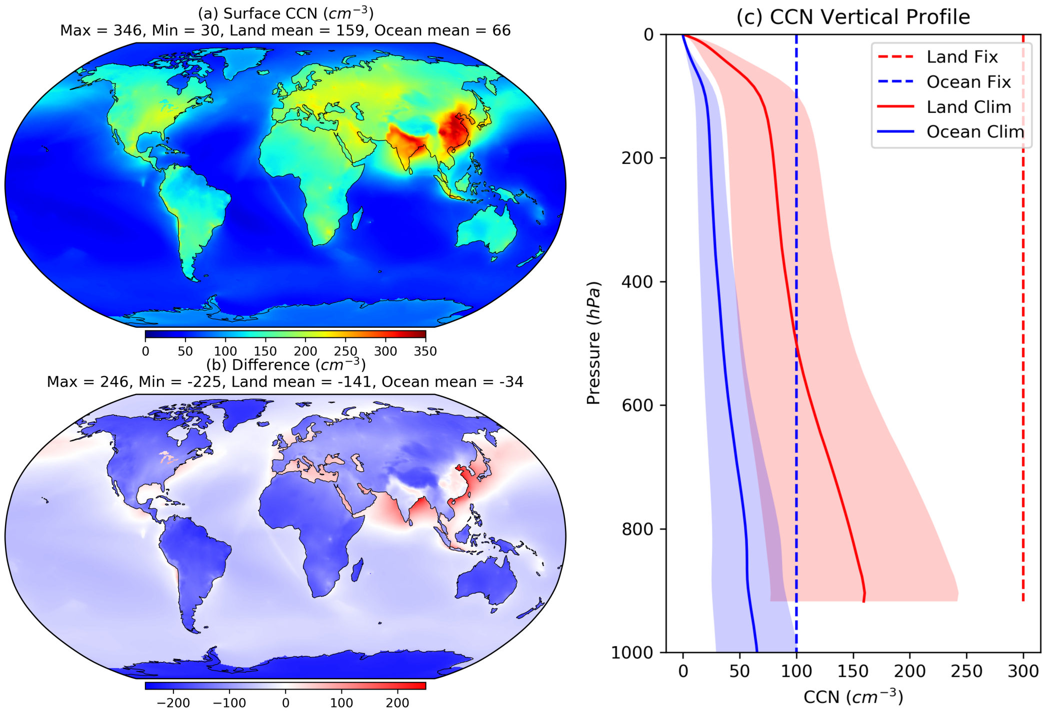

Figure 4. Geographic distribution of (a) surface climatological CCNs (cm^{-3}) from MERRA2, (b) the difference between the CCNs from MERRA2 and the fixed CCNs values used in the GFDL MP v2. Panel (c) is the vertical profiles of (solid) climatological CCNs from MERRA2 and (dashed) fixed CCNs values used in the GFDL MP v2. Red lines represent CCNs over land, blue lines represent CCNs over the ocean. The shaded area is its standard deviation. The numbers in panels (a) and (b) are the global maximum, minimum, land mean, and ocean mean of CCNs.

in the GFDL MP v2. The CCN over land is only half of 300 cm^{-3} near the surface and lower than 100 cm^{-3} above 500 hPa. The CCNs over the ocean is generally half value or lower than the fixed value of 100 cm^{-3}.

4 Model Verification

In order to demonstrate the impact of the GFDL MP upgrade, 10-day weather prediction from SHiELD are evaluated. These predictions are initialized from GFS v15 analyses every five days from June 25, 2019 to March 17, 2021. The ERA5 reanalysis (Hersbach et al., 2020) is then used for global weather prediction evaluation. ERA5 is produced using 4D-Var data assimilation and model forecasts in CY41R2 of the European Centre for Medium-Range Weather Forecasts (ECMWF) Integrated Forecast System (IFS), with 137 hybrid sigma/pressure (model) levels in the vertical and the top-level at 0.01 hPa. Here the 31 km 6 hourly ERA5 datasets at the pressure levels of 100 hPa, 200 hPa, 250 hPa, 500 hPa, 700 hPa, 850 hPa, and 1000 hPa are used to represent the weather and atmospheric condition from Tropopause to the surface. Here we focus on geopotential height, air temperature, and specific humidity, which are of the greatest value to large-scale weather prediction. All experiments done for this study are listed in Table 2. This section compares the GFDL MP v3 (CTRL for short hereafter; this configuration uses constant CCNs over the land and ocean respectively and the original PSD for all cloud

Table 2. List of experiments in this study.

Experiment	Old PSD[1]	Old CCNs[2]	New PSD[3]	New CCNs[4]	GFDL MP
OLD	×	×			v2
CTRL	×	×			v3
CPSD		×	×		v3
AERO	×			×	v3
CPSD_AERO			×	×	v3

[1] mono-dispersed for cloud water and cloud ice, exponential distribution for other cloud categories. [2] 300 cm^{-3} over land and 100 cm^{-3} over ocean. [3] gamma distribution for all cloud categories. [4] CCNs are calculated from climatological aerosol.

categories) with the GFDL MP v2 (OLD for short hereafter). In the following section, the CTRL is used as a reference to evaluate the weather prediction skill of the GFDL MP v3. CTRL is compared against simulations with the more realistic gamma particle size distribution of cloud water and cloud ice (CPSD), a time-and-space varying climatological background aerosol for CCNs calculation (AERO), and simulations with both (CPSD_AERO).

Figure 5 shows a straightforward comparison between the OLD and the CTRL using a scorecard. The scorecard clearly shows that the CTRL has significantly higher anomaly correlation coefficients (ACCs) of geopotential height at most pressure levels up to seven days of forecast. The reduction of geopotential height bias from the OLD to the CTRL is significant even throughout the ten days of forecast. Although the ACCs of the CTRL are lower than those of the OLD after day seventh, this difference is insignificant. The above improvement of geopotential height prediction (higher ACC of geopotential height) is encouraging for the development of SHiELD because it indicates a general improvement of the atmospheric circulation and heating in the Troposphere, which is closely related to our daily weather. It is also found in Figure 5 that the temperature prediction of the CTRL is overall better than the OLD. Still, the ACCs are higher in the first few days and lower in the eight to ten-day forecast, while the bias is significantly reduced throughout the ten-day forecast. Unfortunately, temperature prediction at 500 hPa and 1000 hPa are degraded in the CTRL (lower ACC and larger bias). Further analyses on the 10-day temperature evolution and its 10-day averaged geographical distribution (see supplemental Figures S1, S2) show a globally warm bias at 500 hPa and 1000 hPa. Since the CTRL predicts an overall warmer Troposphere than the OLD and the 500 hPa and 1000 hPa temperature in the OLD already have a positive bias, the additional warming further increases the positive bias at these two pressure levels. Specific humidity prediction is overall better at the upper Troposphere but worse at the lower Troposphere comparing the CTRL to the OLD, shown in the scorecard. However, compared to the magnitude and variation of specific humidity throughout the ten days of forecasts, their difference at the lower Troposphere is small, so that can be negligible (see supplemental Figures S1, S2).

To evaluate the representation of the mean state of cloud prediction, we compare the output from COSP (Cloud Feedback Model Intercomparison Project Observation Simulator Package, Bodas-Salcedo et al. (2011); Swales et al. (2018)) of SHiELD against CALIPSO (Cloud-Aerosol Lidar and Infrared Pathfinder Satellite Observation, Chepfer et al. (2010)) cloud fraction product. The COSP takes the models representation of the atmosphere (e.g., cloud water content at model levels) and simulates the retrievals for several passive and active sensors (e.g., CALIPSO) (Bodas-Salcedo et al., 2011). The output from COSP can then be directly compared with satellite observations. Version 2 of COSP (Swales et al., 2018), a significant reorganization and modernization of the pre-

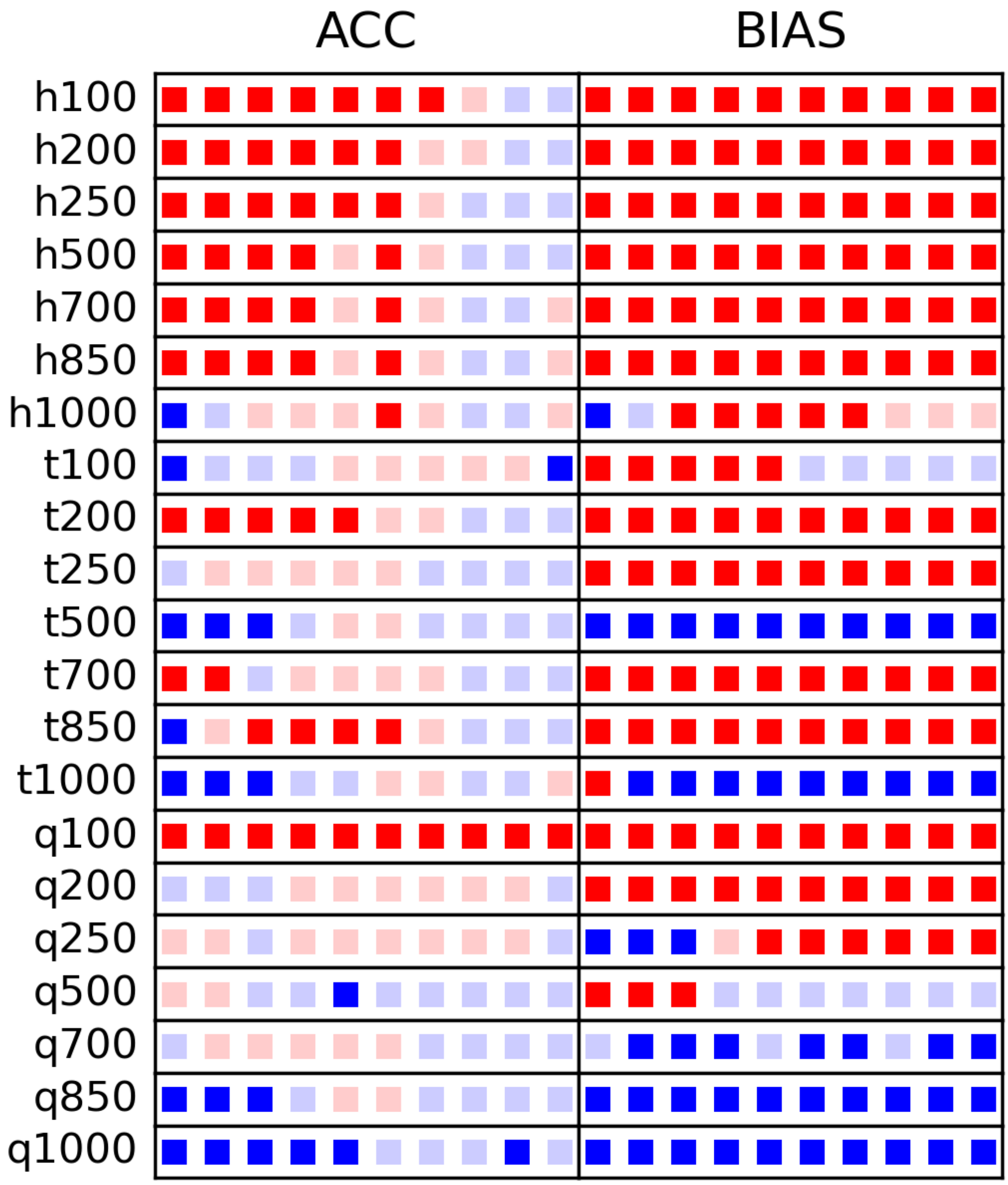

Figure 5. The scorecard showing the comparisons between the GFDL MP v3 (CTRL) and the GFDL MP v2 (OLD) in each meteorological field. Improvements (degradation) from the CTRL are indicated in red (blue) squares, e.g., higher (lower) ACC (anomaly correlation coefficient) or less (larger) bias. Darker colors mean the difference passes the 95% significance level. Square boxes in each grid cell from left to right are for the forecasts from day 1 to day 10. The letters h, t, and q to the left represent geopotential height, temperature, and specific humidity, respectively, at pressure levels of 100, 200, 250, 500, 700, 850, and 1000 hPa.

vious generation of COSP, has been recently implemented into SHiELD for comprehensive cloud evaluation. The CALIPSO data is from the GCM-Oriented CALIPSO Cloud Product (CALIPSO-GOCCP) `https://climserv.ipsl.polytechnique.fr/cfmip-obs/Calipso_goccp.html` that is designed to evaluate GCM (General Circulation Model) cloudiness. CALIPSO-GOCCP (Chepfer et al., 2010) contains observational cloud diagnostics entirely consistent with the ones simulated by the ensemble "GCM+lidar simulator" which has been built in using the same horizontal and vertical resolutions and the same cloud detection thresholds. The lidar simulator is part of COSP. In this study, the total column cloud liquid water, rainwater, cloud ice water, and snow water from ERA5 is also used to evaluate the liquid and ice water paths predicted in SHiELD. Note that graupel is not included in ERA5. Here, total column cloud liquid water and rainwater are combined as liquid water path, and total column cloud ice water and snow water are combined as ice water path. Finally, precipitation prediction is evaluated against the Integrated Multi-satellitE Retrievals for GPM (IMERG) product (Hong et al., 2004), which combines information from the Global Precipitation Measurement (GPM) satellite constellation to estimate precipitation over the majority of the Earth's surface.

Figure 6 shows the cloud fraction comparison between model prediction and CALIPSO observation. As shown in Figure 6e, the OLD predicts similar geographical distribution and magnitude of high cloud fraction as CALIPSO. The predicted global mean high cloud fraction is slightly smaller than that of the CALIPSO (with a bias of -0.006). As shown in Figure 6i, the global mean bias further reduces to 0.001 (positive) in the CTRL, but the root-mean-square error (rmse) remains the same. It can be found in the high cloud fraction difference panel (Figure 6m) that a significant difference in high cloud fraction is over the tropics ocean area. Different from the high cloud fraction, both middle and low cloud fractions are under-predicted in both the OLD and the CTRL (Figure 6f,g,j,k). As shown in Figure 6f,j, the predicted middle cloud fraction is consistently lower in the model than CALIPSO, with a maximum reduction of cloud fraction over Southern America. Comparing the OLD and the CTRL, the upgrade of GFDL MP does not improve the middle cloud fraction prediction too much. Still, the global mean bias and rmse of the predicted middle cloud fraction are both reduced. As shown in Figure 6n, most of the significant middle cloud fraction increment is in the middle to high latitude ocean area, especially the Southern Ocean. Compared to the middle cloud fraction bias, the low cloud fraction bias is even larger (Figure 6g,k). The global mean bias of low cloud fraction is -0.194 and -0.197 in the OLD and the CTRL, respectively. As shown in Figure 6o, most significant reduction of low cloud fraction in the CTRL is over the high latitude land area. Due to the under-prediction of middle and low cloud fractions, the total cloud fraction is also under-predicted (Figure 6h,i). Still, we can see that the global mean bias and rmse of total cloud fraction is reduced because of significant total cloud increment over the Southern Ocean (Figure 6p).

We further evaluate the liquid and ice water paths (compared with ERA5) and precipitation (compared with GPM) predictions. As shown in Figure 7a,d,g, SHiELD's predicted liquid water path is quite similar to ERA5 regarding its geographical distribution. However, both the OLD and the CTRL over-predict the liquid water path over the extratropical storm track area. Compared with the OLD, the bias and rmse in the CTRL are both notably reduced. As shown in Figure 7j, most of the significant reduction of liquid water path is at the middle to high latitudes, where the model over-predicts the liquid water path. Compared with the ERA5, the geographical distributions of the ice water path are well-predicted in both the OLD and the CTRL (Figure 7b,e,h). The bias and rmse of the CTRL are only slightly smaller than that of the OLD. Not surprisingly, the difference between the OLD and the CTRL is insignificant, shown from the difference panel of Figure 7k. Regarding the precipitation forecasts (Figure 7f,i), both the OLD and the CTRL can well-predict the massive precipitation rates along the Intertropical Convergence Zone (ITCZ) area and in the extra-tropical storm track area. However, both the OLD and the CTRL predict slightly more precipitation globally, indicated by their

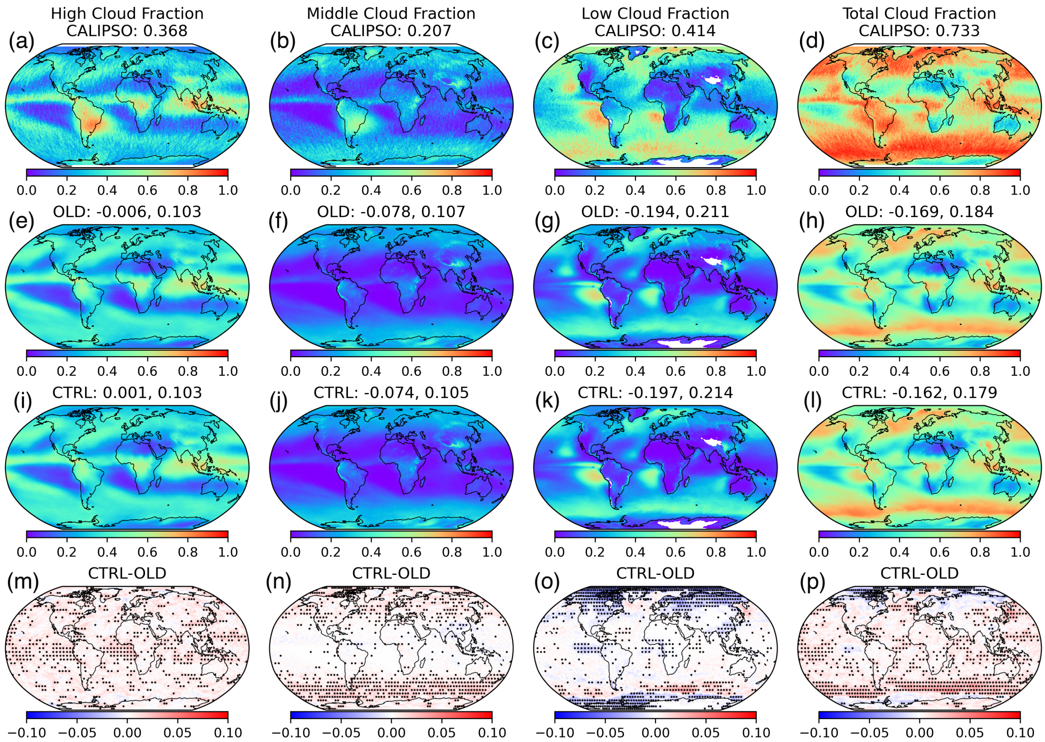

Figure 6. From left to right are the 10-day averaged high, middle, low, and total cloud fractions from (a-d) CALIPSO, (e-h) OLD, (i-l) CTRL, and (m-p) CTRL minus OLD. The numbers in the title of (a-d) are the global mean of cloud fraction (unit: 1), and (e-l) are the bias and root-mean-square error compared to CALIPSO. The dotted area in (m-p) is the area with a 95% significant difference.

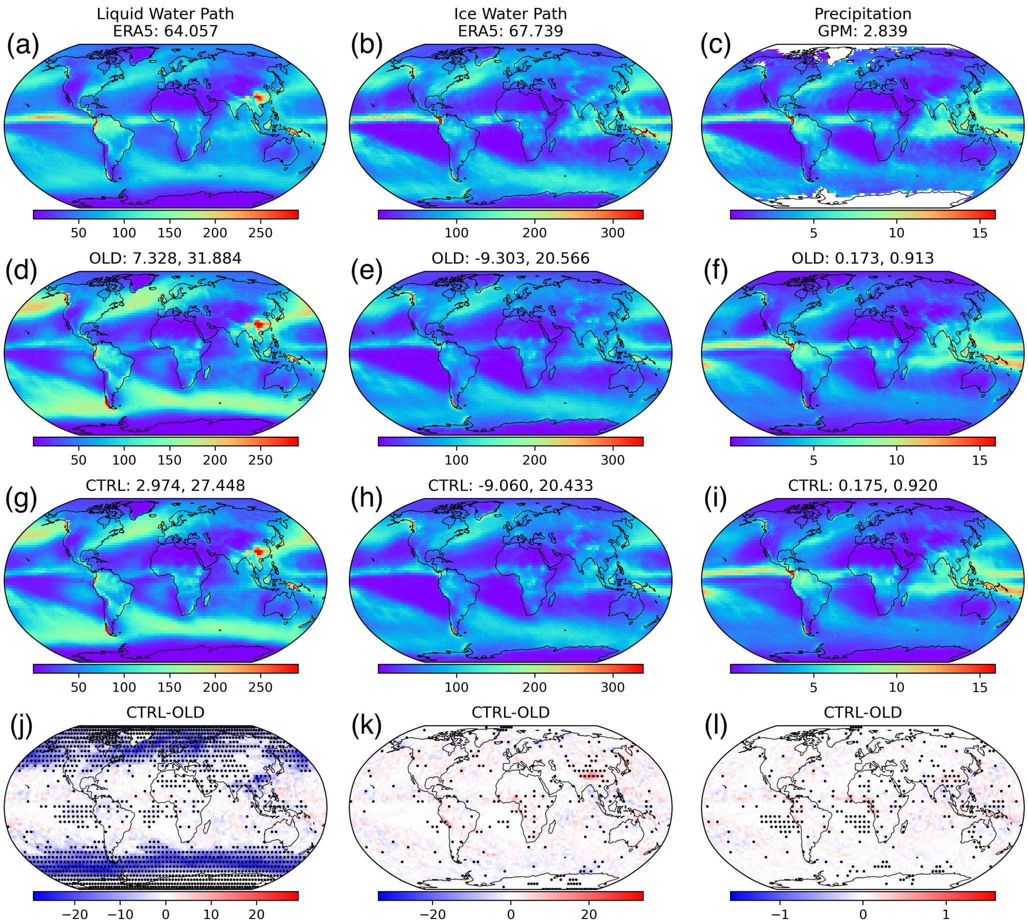

Figure 7. From left to right are the 10-day averaged liquid water path (LWP), ice water path (IWP), and precipitation rate (PRE) from (a-c) ERA5 or GPM, (d-f) OLD, (g-i) CTRL, and (j-l) CTRL minus OLD. The numbers in the title of (a-c) are the global mean of liquid water path or ice water path (unit: $g\ m^{-2}$) or precipitation (unit: $mm\ day^{-1}$), and (d-i) are the bias and root-mean-square error to ERA5 or GPM. The dotted area in (j-l) is the area with a 95% significant difference.

global mean bias. The CTRL's precipitation prediction has a slightly larger bias and rmse than the OLD, but the differences are insignificant (Figure 7l).

5 Impacts of PSD and CCNs on Weather Prediction

The previous section demonstrates the results from the GFDL MP upgrade that excludes the more realistic particle size distribution (PSD) and new cloud condensation nuclei (CCNs). In the CTRL, the PSD of cloud water and cloud ice is still mono-dispersed, and the CCNs are constant values over land and ocean separately. CTRL generally improves the prediction skill of geopotential height and reduces biases in height, temperature, and liquid water path, but had relatively little change to cloud biases. In this section, three sensitivity experiments(CPSD, AERO, and CPSD_AERO) are carried out to evaluate the impacts (or effect) of the PSD in the GFDL MP v3, as well as the use of time-and-space varying prescribed climatological aerosol to calculate CCNs, on weather prediction. Those new experiments are listed in Table 2. Experiment CPSD is designed

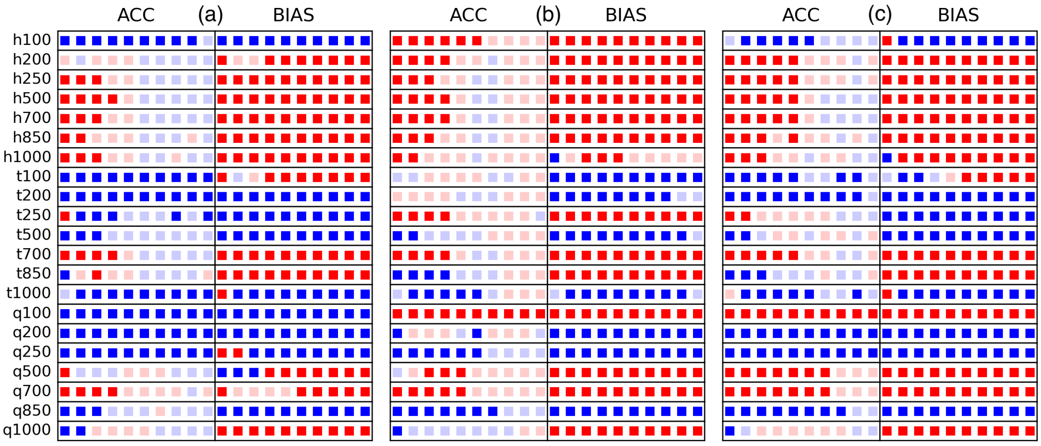

Figure 8. Similar to Figure 5, but for comparison between (a) CTRL and CPSD, (b) CTRL and AERO, (c) CTRL and CPSD_AERO.

based on the CTRL with a more realistic PSD of cloud water and cloud ice using the gamma distribution. Terminal velocity, effective radius, and a number of microphysical processes are revised accordingly, as described in Section 3. Experiment AERO is also designed based on the CTRL, but with the CCNs replaced with those calculated from the MERRA2 climatological aerosol. CCNs are mainly used for cloud water to rainwater autoconversion in the GFDL MP. The last experiment is a combination of the CPSD and the AERO experiments, called the CPSD_AERO. Comparisons between the CTRL and each of the three experiments use ERA5, CALIPSO, and GPM mentioned in the previous section.

The scorecards of the comparison between the CTRL and each of the sensitivity experiments are in Figure 8. It can be found that the ACCs of geopotential height in the CPSD are higher than those in the CTRL in the first five-day forecast. Meanwhile, compared to the CTRL, the biases of geopotential height prediction are significantly smaller throughout the ten-day forecast (Figure 8a). On the other hand, the temperature and specific humidity predictions in the CPSD are generally improved at levels lower than 500 hPa but significantly degraded at 500 hPa and above. The differences of the temperature ACC between the CPSD and CTRL are hard to quantify in the time evolution plots, but their difference of temperature biases are quite clear (see supplemental Figure S3). Compared to the CTRL, the predicted temperature in the CPSD is lower at 200 and 250 hPa, but higher at 500 hPa, and the predicted specific humidity in the CPSD is lower at 100, 200, and 250 hPa.

To understand why the temperature and specific humidity decrease at the middle to upper Troposphere (except that temperature at 500 hPa increases) in the CPSD than the CTRL, we first examine the cloud fraction prediction (Figure 9). The CPSD predicted a similar amount of high cloud fraction to the CTRL (Figure 9e). The high cloud fraction prediction bias is very close between the CPSD and the CTRL. The rmse of the high cloud fraction prediction in the CPSD is slightly larger than that of the CTRL throughout the ten-day forecast (Figure 9a). In contrast, there is a much more significant increment of the rmse of middle cloud fraction prediction from the CTRL to the CPSD (Figure 9b). Comparing the bias of middle cloud fraction prediction shown in Figure 9f, we can see the predicted middle cloud fraction is significantly more in the CPSD than the CTRL. It implies that more water vapor deposited to cloud ice to form middle clouds in the CPSD. The associated latent heating warms up the air in the middle Troposphere.

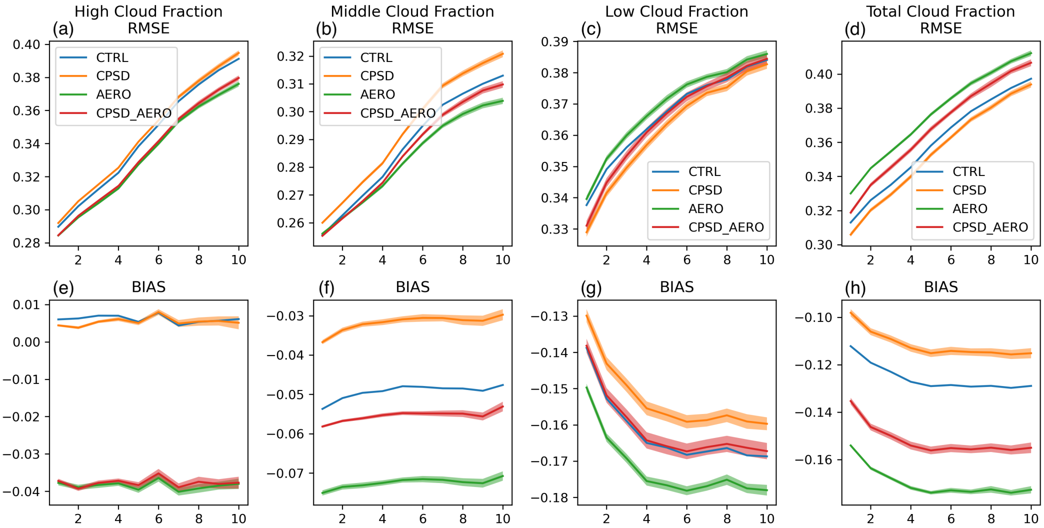

Figure 9. From left to right are the 10-day evolution of (a,e) high, (b,f) middle, (c,g) low, and (d,h) total cloud fractions of (blue) CTRL, (orange) CPSD, (green) AERO, and (red) CPSD_AERO. Top row is root mean square error (unit: 1); bottom row is bias (unit: 1). The shaded area is the area with a 95% significant difference to the CTRL.

Due to the decrease of the water vapor in the upper Troposphere, the longwave radiation absorption reduces; meanwhile, the increasing middle cloud fraction enhances the cloud top cooling in the above air, the atmospheric temperature is decreased in the CPSD compared to the CTRL. These are consistent with what we found in the temperature and specific humidity prediction in Figure 8a.

The increases of the predicted cloud ice in the CPSD are also shown by the ice water path (Figure 10e). The ice water path prediction bias changes from negative to positive from the CTRL to the CPSD. The absolute ice water path prediction bias is relatively smaller in the CPSD compared to the CTRL. However, the rmse of ice water path prediction increases significantly (Figure 10b). The predicted ice water path dramatically increases from the CTRL to the CPSD because of the increases of the cloud ice terminal fall velocity in the CPSD with the redefinition of cloud ice PSD. As a result, it brings more cloud ice sediment to lower levels, while the reduction of cloud ice at higher levels causes more deposition of water vapor. The improvement of low cloud fraction prediction (Figure 9c,g) probably contributes to the improvement of the temperature and specific humidity prediction in the lower Troposphere (Figure 8a). The degradation of the precipitation prediction is small in CPSD (Figure 10c,f).

The upgrade of the CCNs calculation in the AERO directly affects the autoconversion of cloud water to rainwater. Figure 8b shows that the prediction skill of geopotential height, temperature, and specific humidity are generally improved. Particularly, the ACCs of geopotential height substantially increase with significant bias reductions. Due to less produced CCNs in the AERO than the CTRL, it is relatively easier for the cloud water to convert to rain and fall to the surface in the AERO than in the CTRL. Therefore, the low cloud fraction in the AERO is largely reduced (Figure 9g), and the liquid water path is also significantly reduced (Figure 10d). The reduction of cloud fraction and the resultant reduced cloud albedo lead to a warmer surface. With a stronger surface heat exchange, the lower Troposphere is warmed up. Extra heat is transported from the lower Troposphere to the air above, inducing a warmer middle to upper Troposphere. It is relatively harder for the water vapor to condense or deposit in the warmer

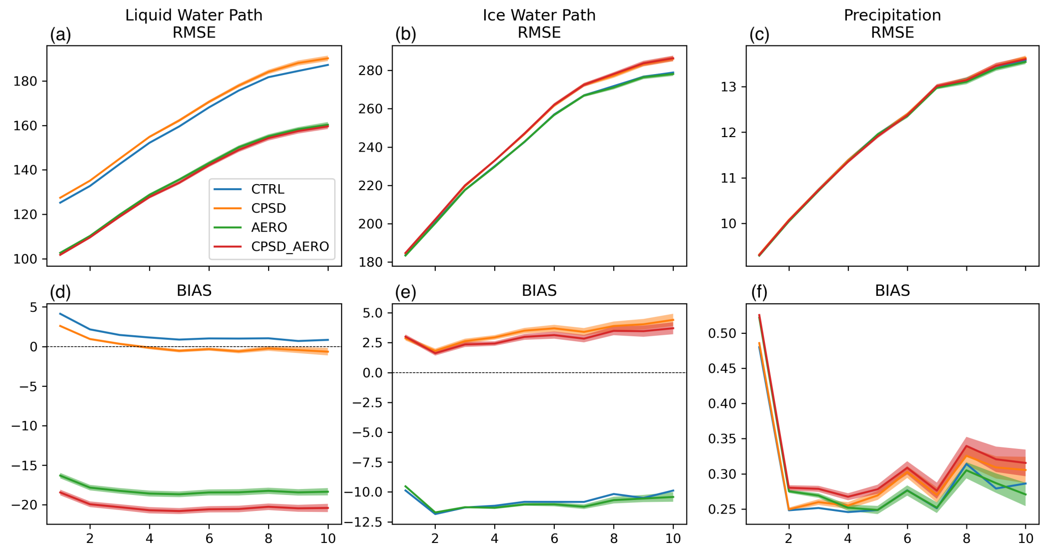

Figure 10. From left to right are the 10-day evolution of (a,d) liquid water path, (b,e) ice water path, and (c,f) precipitation of (blue) CTRL, (orange) CPSD, (green) AERO, and (red) CPSD_AERO. Top row is root mean square error (unit: $g\ m^{-2}$); bottom row is bias (unit: $g\ m^{-2}$). The shaded area is the area with a 95% significant difference to the CTRL.

air. Therefore, the high and middle cloud fractions (Figure 9e, f) further decrease. Even with more cloud water to rain autoconversion in the AERO than the CTRL, the changes of precipitation prediction are still minor (Figure 10c,f), which may be related to some compensation from the increase of convective precipitation.

Finally, the impacts of combining the more realistic PSD and the climatological aerosol calculated CCNs are evaluated (Exp. of CPSD_AERO). Figure 8c shows that the AERO can improve the degradation of the forecast skill shown in the CPSD. For example, the forecasts of the geopotential height of the CPSD_AERO during the first 5 days are significantly improved compared to the CTRL. Moreover, temperature forecasts at 250 and 500 hPa, and forecasts of specific humidity at 100, 500, and 700 hPa are generally improved in the CPSD_AERO. Generally speaking, there are more improved forecast fields than degraded ones in the CPSD_AERO than in the CTRL (Figure 8c). It is interesting to find in Figure 9 that the high cloud fraction prediction in the CPSD_AERO is quite close to the AERO, but the middle, low, and total cloud fraction prediction in the CPSD_AERO is in between the CPSD and the AERO. Differently, the prediction of the liquid water path of the CPSD_AERO is close to the AERO, but the ice water path of the CPSD_AERO is close to the CPSD. Since the update of the PSD alters many microphysical processes, but the update of the CCNs changes the cloud water to rainwater autoconversion only, it is difficult to explain these interesting findings. We leave these to further research.

In all experiments, we find that the change of PSD in the cloud water and the cloud ice or the use of climatological aerosol for CCNs calculation only exerts a minor impact on the precipitation prediction (Figure 10c,f). It is possibly due to the change of large-scale precipitation being small compared to the change of cloud content. In addition, the change of the large-scale precipitation could be compensated by an increase in convective precipitation. Additionally, precipitation can be influenced by microphysical processes that do not involve the change of PSD and CCNs.

6 Summary and Discussion

This paper documents the third version of the Geophysical Fluid Dynamics Laboratory cloud microphysics scheme (GFDL MP v3) that is upgraded from the previous versions of the GFDL MP used in the Global Forecast System (GFS), the System for High-resolution prediction on Earth-to-Local Domains (SHiELD), and a broader community through the Unified Forecast System (UFS). Compared with the GFDL MP v2, the GFDL MP v3 is featured with the following upgrades: 1) the code has been reorganized, optimized, and modularized by functions; 2) the particle size distribution used in the scheme for all six cloud categories are redefined as gamma distribution; 3) particle concentration, effective diameter, optical extinction, mass mixing ratio, radar reflectivity factor, and terminal velocity are all redefined based on the gamma distribution; 4) accretion, evaporation, sublimation, deposition, melting, and freezing microphysical processes are all reformulated based on the gamma distribution; 5) replacing uniform cloud condensation nuclei (CCNs) with climatological aerosols calculated from Modern-Era Retrospective analysis for Research and Applications, version 2 (MERRA2). The GFDL MP v3 ensures an overall microphysical consistency and easily permits the future introduction of new particle size distributions, microphysical processes, and multi-moment distributions.

The impacts of the GFDL MP upgrade item 1) on global weather, cloud, and precipitation predictions in SHiELD are comprehensively evaluated. The comparisons between the two sets of experiments show that GFDL MP v3 significantly improves the geopotential height prediction up to seven days on anomaly correlation coefficient (ACC) and throughout ten-day forecast on the bias. Improvement of geopotential height prediction indicates general improvement of the atmospheric circulation and heating in the Troposphere. The temperature prediction is overall better in GFDL MP v3 than in GFDL MP v2. The specific humidity prediction is overall better in GFDL MP v3 than GFDL MP v2 in the upper Troposphere but worse in the lower Troposphere. High, middle, and total cloud fractions predictions are improved in GFDL MP v3. Low cloud fraction prediction degrades in GFDL MP v3, but liquid water path prediction improves substantially. There is a minor change in the ice water path and precipitation prediction from GFDL MP v2 and GFDL MP v3. It is believed that the noticed degradation could be improved with further model development.

Furthermore, the impacts of the GFDL MP upgrade items 2) to 5) are evaluated using the base GFDL MP v3 as a reference. The use of more realistic PSD and climatological aerosol calculated CCNs significantly improves the geopotential height prediction compared with the original PSD and constant CCNs. Temperature and specific humidity predictions at the upper Troposphere significantly degrade with the PSD upgrade, but are mixed with improvement and degradation with the CCNs upgrade. Among all upgrades, the PSD upgrade shows the best prediction of low and total cloud fractions but the worst prediction of high and middle cloud fractions, while the CCNs upgrade shows the best prediction of high and middle cloud fractions but the worst prediction of low and total cloud fractions. The combination of the PSD and the CCNs upgrades is generally excellent in cloud fraction prediction. The combination of the PSD and the CCNs upgrades shows the best liquid water path prediction with the lowest rmse, but with a very large negative bias. The PSD upgrade shows the largest rmse of liquid water path prediction, although its bias is the smallest. In contrast, the combination of the PSD and the CCNs upgrades shows the smallest bias in ice water path prediction but a larger rmse of the ice water path prediction. These results indicate that the global mean liquid and ice water paths are very different between the ERA5 and SHiELD. Note that we use ERA5 to evaluate liquid water path and ice water path prediction because this is the only reliable validation dataset available for the entire forecast time period. More reliable direct observations will be used for this purpose in the future.

There are some caveats for the GFDL MP v3. For example, the prediction of 500 hPa temperature tends to be worse (lower ACC and larger warm bias) than the GFDL MP v2. This bias has been identified in SHiELD for a long time. A possible reason is that the convective heating of the middle Troposphere is too strong, and radiative cooling is not enough to compensate. Further investigation is still needed to alleviate this bias. Middle, low, and total cloud fractions are under-predicted in SHiELD regardless of the version of the GFDL MP used. We plan to extend our cloud fraction diagnosis in the GFDL MP to include sub-grid terrain and static energy to better represent subgrid variability especially over complex terrain. We are also working on a more physically-motivated definition of parameters in the particle size distribution using observations from flights and to incorporate the effects of temperature, wind, and pressure on the PSD. This aims to create a more realistic relationship between meteorological fields and particle size distribution from observational data, and to resolve the degradation of upper-tropospheric biases in temperature and humidity. We also plan to eliminate the low bias in low-to-middle latitudes, and high bias in high latitudes, of liquid water path, and to improve the seamlessness of the GFDL MP across space and time scales, as appropriate for the wide range of applications of SHiELD, GFS, and UFS from convective-scale to seasonal prediction. We also will consider a double-moment extension of the GFDL MP if it improves the model's prediction skill.

Appendix A The GFDL Cloud Microphysics Version 3

The third version of the GFDL cloud microphysics scheme (GFDL MP) was developed from version 1 (Zhou et al., 2019) and version 2 (L. Harris, Zhou, Lin, et al., 2020). This new version of the GFDL MP features with three major upgrades: 1) the code is entirely reorganized, optimized, and modularized by functions, 2) there are various scientific modifications to the microphysical processes, and 3) several optional definitions and microphysical processes are added. The scientific modifications are summarized as below:

- Redefine the supersaturation in ice processes using the complete saturation tables (it is advance and ensures consistency);
- Allow cloud water autoconversion in a larger temperature range (it is consistent with the temperature range of cloud water);
- Split rain evaporation and accretion more physically and consistently (it more physically handles the relation between rain evaporation and accretion);
- Turn off the redundant cloud ice melting before falling (the same process is already in the ice microphysics section);
- Fix and revise the cloud ice melting processes during sedimentation (a bug was found in these processes, not used by default);
- Remove several unnecessary temperature limits and add necessary mass limits (some temperature limits are reasonably defined; mass limits prevent negative cloud mass)
- Use the same minimum value for all hydrometeors (to be consistent);
- Recalculate the parameters for terminal fall (for better precision and ease for future development);
- Allow zero fall speed (instead of a small value; it is more physical);
- Remove time step splitting between fast saturation adjustment and full microphysics (it is more reasonable in the current structure);
- Combine snow and graupel for snow effective radius diagnosis (to include the radiative effect of graupel);
- When it is cloud water saturation adjustment, do it completely (by design).

There are also many options added to the GFDL MP that can be used in other applications of SHiELD (T-SHiELD, C-SHiELD, and S-SHiELD), toward unified modeling in which there is a single modeling system with one code, one executable, and one workflow (L. Harris, Zhou, Lin, et al., 2020). Those new options include:

- New cloud fraction diagnostic schemes;
- New cloud ice nucleation schemes;
- New cloud ice generation schemes;
- New cloud ice fall velocity diagnostic schemes;
- New cloud water and cloud ice effective radii diagnostic schemes;
- New radar reflectivity diagnostic schemes;
- Wegener-Bergeron-Findeisen process;
- New particle size distribution options;
- New cloud condensation nuclei calculation.

Data Availability Statement

The source codes of SHiELD are available at `https://doi.org/10.5281/zenodo.5800223`. The corresponding data is available at `https://doi.org/10.5281/zenodo.5800259`. The COSP2 software package can be accessed from `https://github.com/CFMIP/COSPv2.0`.

The MERRA2 data can be obtained from `https://goldsmr5.gesdisc.eosdis.nasa.gov/data`. The ERA5 data can be obtained from `https://cds.climate.copernicus.eu/#!/search?text=ERA5&type=dataset`. The CALIPSO-GOCCP data can be obtained from `https://climserv.ipsl.polytechnique.fr/cfmip-obs/Calipso_goccp.html`. The GPM data can be obtained from `https://disc.gsfc.nasa.gov/datasets/GPM_3IMERGHH_06/summary?keywords=gpm%20imerg`.

Acknowledgments
The authors want to thank Dr. Shian-Jiann Lin, who developed the early version of the GFDL cloud microphysics scheme more than ten years ago. His great ideas and philosophy are still in the latest version of this scheme. Many thanks also go to the GFDL FV3 team, who support the development of the GFDL MP in many ways. The authors also want to thank Dr. Songmiao Fan, Dr. Zhihong Tan, and Dr. Nadir Jeevanjee for their valuable comments and suggestions to improve the quality of this manuscript.

References

Arnold, N. P., Putman, W. M., & Freitas, S. R. (2020). Impact of resolution and parameterized convection on the diurnal cycle of precipitation in a global nonhydrostatic model [Journal Article]. *Journal of the Meteorological Society of Japan. Ser. II*, *98*(6), 1279-1304. doi: 10.2151/jmsj.2020-066

Baldauf, M., Seifert, A., Forstner, J., Majewski, D., Raschendorfer, M., & Reinhardt, T. (2011). Operational convective-scale numerical weather prediction with the cosmo model: Description and sensitivities [Journal Article]. *Monthly Weather Review*, *139*(12), 3887-3905. doi: 10.1175/Mwr-D-10-05013.1

Bauer, P., Thorpe, A., & Brunet, G. (2015). The quiet revolution of numerical weather prediction [Journal Article]. *Nature*, *525*(7567), 47-55. doi: 10.1038/nature14956

Beard, K. V., & Pruppacher, H. R. (1971). A wind tunnel investigation of the rate of evaporation of small water drops falling at terminal velocity in air [Journal Article]. *Journal of the Atmospheric Sciences*, *28*(8), 1455-1464. doi: 10.1175/1520-0469(1971)028⟨1455:Awtiot⟩2.0.Co;2

Bigg, E. K. (1953). The supercooling of water [Journal Article]. *Proceedings of the Physical Society. Section B*, *66*(8), 688-694. doi: 10.1088/0370-1301/66/8/

309

Bodas-Salcedo, A., Webb, M. J., Bony, S., Chepfer, H., Dufresne, J. L., Klein, S. A., ... John, V. O. (2011). Cosp satellite simulation software for model assessment [Journal Article]. *Bulletin of the American Meteorological Society*, *92*(8), 1023-1043. doi: 10.1175/2011bams2856.1

Boucher, O., & Lohmann, U. (1995). The sulfate-ccn-cloud albedo effect - a sensitivity study with 2 general-circulation models [Journal Article]. *Tellus Series B-Chemical and Physical Meteorology*, *47*(3), 281-300. doi: 10.1034/j.1600-0889.47.issue3.1.x

Byers, H. R. (1965). *Elements of cloud physics* [Book]. Chicago: University of Chicago Press.

Chen, J., Lin, S., Magnusson, L., Bender, M., Chen, X., Zhou, L., ... Harris, L. (2019). Advancements in hurricane prediction with noaa's next-generation forecast system [Journal Article]. *Geophysical Research Letters*, *46*(8), 4495-4501. doi: 10.1029/2019gl082410

Chen, J. H., & Lin, S. J. (2011). The remarkable predictability of inter-annual variability of atlantic hurricanes during the past decade [Journal Article]. *Geophysical Research Letters*, *38*(11), n/a-n/a. doi: 10.1029/2011gl047629

Chen, J. H., & Lin, S. J. (2013). Seasonal predictions of tropical cyclones using a 25-km-resolution general circulation model [Journal Article]. *Journal of Climate*, *26*(2), 380-398. doi: 10.1175/Jcli-D-12-00061.1

Chen, J. H., Lin, S. J., Zhou, L. J., Chen, X., Rees, S., Bender, M., & Morin, M. (2019). Evaluation of tropical cyclone forecasts in the next generation global prediction system [Journal Article]. *Monthly Weather Review*, *147*(9), 3409-3428. doi: 10.1175/Mwr-D-18-0227.1

Chepfer, H., Bony, S., Winker, D., Cesana, G., Dufresne, J. L., Minnis, P., ... Zeng, S. (2010). The gcm-oriented calipso cloud product (calipso-goccp) [Journal Article]. *Journal of Geophysical Research*, *115*(D4). doi: 10.1029/2009jd012251

Dong, J., Liu, B., Zhang, Z., Wang, W., Mehra, A., Hazelton, A. T., ... Marks, F. (2020). The evaluation of real-time hurricane analysis and forecast system (hafs) stand-alone regional (sar) model performance for the 2019 atlantic hurricane season [Journal Article]. *Atmosphere*, *11*(6). doi: 10.3390/atmos11060617

Ek, M. B., Mitchell, K. E., Lin, Y., Rogers, E., Grunmann, P., Koren, V., ... Tarpley, J. D. (2003). Implementation of noah land surface model advances in the national centers for environmental prediction operational mesoscale eta model [Journal Article]. *Journal of Geophysical Research-Atmospheres*, *108*(D22), n/a-n/a. doi: 10.1029/2002jd003296

Fan, J. W., Wang, Y., Rosenfeld, D., & Liu, X. H. (2016). Review of aerosol-cloud interactions: Mechanisms, significance, and challenges [Journal Article]. *Journal of the Atmospheric Sciences*, *73*(11), 4221-4252. Retrieved from `<GotoISI>://WOS:000386007800001` doi: 10.1175/Jas-D-16-0037.1

Federer, B., & Waldvogel, A. (1975). Hail and raindrop size distributions from a swiss multicell storm [Journal Article]. *Journal of Applied Meteorology*, *14*(1), 91-97. doi: 10.1175/1520-0450(1975)014⟨0091:Harsdf⟩2.0.Co;2

Forbes, R., & Tompkins, A. (2011). An improved representation of cloud and precipitation [Meteorology]. , 13-18. doi: 10.21957/nfgulzhe

Forbes, R., Tompkins, A., & Untch, A. (2011, 09). A new prognostic bulk microphysics scheme for the ifs. (649), 22. doi: 10.21957/bf6vjvxk

Fu, Q. A. (1996). An accurate parameterization of the solar radiative properties of cirrus clouds for climate models [Journal Article]. *Journal of Climate*, *9*(9), 2058-2082. doi: 10.1175/1520-0442(1996)009⟨2058:Aapots⟩2.0.Co;2

Gao, K., Chen, J. H., Harris, L. M., Lin, S. J., Xiang, B. Q., & Zhao, M. (2017). Impact of intraseasonal oscillations on the tropical cyclone activity over the gulf of mexico and western caribbean sea in gfdl hiram [Journal Article].

Journal of Geophysical Research-Atmospheres, *122*(24), 13125-13137. doi: 10.1002/2017jd027756

Gao, K., Harris, L., Chen, J. H., Lin, S. J., & Hazelton, A. (2019). Improving agcm hurricane structure with two-way nesting [Journal Article]. *Journal of Advances in Modeling Earth Systems*, *11*(1), 278-292. doi: 10.1029/2018ms001359

Gelaro, R., McCarty, W., Suarez, M. J., Todling, R., Molod, A., Takacs, L., ... Zhao, B. (2017). The modern-era retrospective analysis for research and applications, version 2 (merra-2) [Journal Article]. *J Clim*, *Volume 30*(Iss 13), 5419-5454. doi: 10.1175/JCLI-D-16-0758.1

Gunn, K. L. S., & Marshall, J. S. (1958). The distribution with size of aggregate snowflakes [Journal Article]. *Journal of Meteorology*, *15*(5), 452-461. doi: 10.1175/1520-0469(1958)015⟨0452:Tdwsoa⟩2.0.Co;2

Guo, H., Ming, Y., Fan, S., Zhou, L., Harris, L., & Zhao, M. (2021). Two-moment bulk cloud microphysics with prognostic precipitation in gfdl's atmosphere model am4.0: Configuration and performance [Journal Article]. *Journal of Advances in Modeling Earth Systems*, *13*(6), e2020MS002453. doi: 10.1029/2020ms002453

Han, J., & Bretherton, C. S. (2019). Tke-based moist eddy-diffusivity mass-flux (edmf) parameterization for vertical turbulent mixing [Journal Article]. *Weather and Forecasting*, *34*(4), 869-886. doi: 10.1175/Waf-D-18-0146.1

Han, J. G., Wang, W. G., Kwon, Y. C., Hong, S. Y., Tallapragada, V., & Yang, F. L. (2017). Updates in the ncep gfs cumulus convection schemes with scale and aerosol awareness [Journal Article]. *Weather and Forecasting*, *32*(5), 2005-2017. doi: 10.1175/Waf-D-17-0046.1

Harris, L., Chen, X., Zhou, L., & Chen, J.-H. (2020). The nonhydrostatic solver of the gfdl finite-volume cubed-sphere dynamical core [Journal Article]. doi: https://doi.org/10.25923/9wdt-4895

Harris, L., Zhou, L., Chen, X., & Chen, J.-H. (2020). The gfdl finite-volume cubed-sphere dynamical core: Release 201912 [Journal Article]. doi: https://doi.org/10.25923/7h88-c534

Harris, L., Zhou, L., Lin, S., Chen, J., Chen, X., Gao, K., ... Stern, W. (2020). Gfdl shield: A unified system for weather-to-seasonal prediction [Journal Article]. *Journal of Advances in Modeling Earth Systems*, *12*(10), e2020MS002223. doi: 10.1029/2020ms002223

Harris, L. M., & Lin, S. J. (2013). A two-way nested global-regional dynamical core on the cubed-sphere grid [Journal Article]. *Monthly Weather Review*, *141*(1), 283-306. doi: 10.1175/Mwr-D-11-00201.1

Harris, L. M., Lin, S. J., & Tu, C. Y. (2016). High-resolution climate simulations using gfdl hiram with a stretched global grid [Journal Article]. *Journal of Climate*, *29*(11), 4293-4314. doi: 10.1175/Jcli-D-15-0389.1

Harris, L. M., Rees, S. L., Morin, M., Zhou, L., & Stern, W. F. (2019). Explicit prediction of continental convection in a skillful variable-resolution global model [Journal Article]. *Journal of Advances in Modeling Earth Systems*, *11*(6), 1847-1869. doi: 10.1029/2018ms001542

Hazelton, A., Alaka, G. J., Cowan, L., Fischer, M., & Gopalakrishnan, S. (2021). Understanding the processes causing the early intensification of hurricane dorian through an ensemble of the hurricane analysis and forecast system (hafs) [Journal Article]. *Atmosphere*, *12*(1). doi: 10.3390/atmos12010093

Hazelton, A. T., Harris, L., & Lin, S. J. (2018). Evaluation of tropical cyclone structure forecasts in a high-resolution version of the multiscale gfdl fvgfs model [Journal Article]. *Weather and Forecasting*, *33*(2), 419-442. doi: 10.1175/Waf-D-17-0140.1

He, B., Bao, Q., Wang, X. C., Zhou, L. J., Wu, X. F., Liu, Y. M., ... Zhang, X. Q. (2019). Cas fgoals-f3-l model datasets for cmip6 historical atmospheric model intercomparison project simulation [Journal Article]. *Advances in Atmospheric Sciences*, *36*(8), 771-778. doi: 10.1007/s00376-019-9027-8

Hersbach, H., Bell, B., Berrisford, P., Hirahara, S., Horanyi, A., Munoz-Sabater, J., ... Thepaut, J. N. (2020). The era5 global reanalysis [Journal Article]. *Quarterly Journal of the Royal Meteorological Society*, *146*(730), 1999-2049. doi: 10.1002/qj.3803

Hoke, J. E., Phillips, N. A., Dimego, G. J., Tuccillo, J. J., & Sela, J. G. (1989). The regional analysis and forecast system of the national meteorological center [Journal Article]. *Weather and Forecasting*, *4*(3), 323-334. doi: 10.1175/1520-0434(1989)004⟨0323:Traafs⟩2.0.Co;2

Hong, Y., Hsu, K.-L., Sorooshian, S., & Gao, X. (2004). Precipitation estimation from remotely sensed imagery using an artificial neural network cloud classification system [Journal Article]. *Journal of Applied Meteorology*, *43*(12), 1834-1853. doi: 10.1175/JAM2173.1

Houze, R. A. (2014). *Cloud dynamics* (Second edition. ed.) [Book]. Amsterdam ; New York: Academic Press is an imprint of Elsevier.

Houze, R. A., Hobbs, P. V., Herzegh, P. H., & Parsons, D. B. (1979). Size distributions of precipitation particles in frontal clouds [Journal Article]. *Journal of the Atmospheric Sciences*, *36*(1), 156-162. doi: 10.1175/1520-0469(1979)036⟨0156:Sdoppi⟩2.0.Co;2

Huang, B., Wang, X., Kleist, D. T., & Lei, T. (2021). A simultaneous multiscale data assimilation using scale-dependent localization in gsi-based hybrid 4denvar for ncep fv3-based gfs [Journal Article]. *Monthly Weather Review*, *149*(2), 479-501. doi: 10.1175/mwr-d-20-0166.1

Ikawa, M., & Saito, K. (1991, 12). *Description of a nonhydrostatic model developed at the forecast research department of the mri* (Technical Report No. 28). Meteorological Research Instituite, Japan: Meteorological Research Instituite, Japan. doi: 10.11483/mritechrepo.28

Jeevanjee, N. (2017). Vertical velocity in the gray zone [Journal Article]. *Journal of Advances in Modeling Earth Systems*, *9*(6), 2304-2316. doi: 10.1002/2017ms001059

Khain, A. P., Beheng, K. D., Heymsfield, A., Korolev, A., Krichak, S. O., Levin, Z., ... Yano, J. I. (2015). Representation of microphysical processes in cloud-resolving models: Spectral (bin) microphysics versus bulk parameterization [Journal Article]. *Reviews of Geophysics*, *53*(2), 247-322. doi: 10.1002/2014rg000468

Kogan, Y. (2013). A cumulus cloud microphysics parameterization for cloud-resolving models [Journal Article]. *Journal of the Atmospheric Sciences*, *70*(5), 1423-1436. doi: 10.1175/Jas-D-12-0183.1

Lamb, D., & Verlinde, J. (2011). *Physics and chemistry of clouds* [Book]. Cambridge ; New York: Cambridge University Press.

Leighton, H., Black, R., Zhang, X. J., Marks, F. D., & Gopalakrishnan, S. G. (2020). Ice particle size distributions from composites of microphysics observations collected in tropical cyclones [Journal Article]. *Geophysical Research Letters*, *47*(15), e2020GL088762. doi: 10.1029/2020GL088762

Li, J., Bao, Q., Liu, Y., Wu, G., Wang, L., He, B., ... Li, J. (2019). Evaluation of famil2 in simulating the climatology and seasonal-to-interannual variability of tropical cyclone characteristics [Journal Article]. *Journal of Advances in Modeling Earth Systems*, *11*(4), 1117-1136. doi: 10.1029/2018ms001506

Lin, S.-J. (2004). A "vertically lagrangian" finite-volume dynamical core for global models [Journal Article]. *Monthly Weather Review*, *132*(10), 2293-2307. doi: 10.1175/1520-0493(2004)132⟨2293:Avlfdc⟩2.0.Co;2

Lin, Y. L., Farley, R. D., & Orville, H. D. (1983). Bulk parameterization of the snow field in a cloud model [Journal Article]. *Journal of Climate and Applied Meteorology*, *22*(6), 1065-1092. doi: 10.1175/1520-0450(1983)022⟨1065:Bpotsf⟩2.0.Co;

2
Liu, J. Y., & Orville, H. D. (1969). Numerical modeling of precipitation and cloud shadow effects on mountain-induced cumuli [Journal Article]. *Journal of the Atmospheric Sciences*, *26*(6), 1283-1298. doi: 10.1175/1520-0469(1969)026⟨1283:Nmopac⟩2.0.Co;2
Marshall, J. S., & Palmer, W. M. (1948). The distribution of raindrops with size [Journal Article]. *Journal of Meteorology*, *5*(4), 165-166. doi: 10.1175/1520-0469(1948)005⟨0165:Tdorws⟩2.0.Co;2
Martin, G. M., Johnson, D. W., & Spice, A. (1994). The measurement and parameterization of effective radius of droplets in warm stratocumulus clouds [Journal Article]. *Journal of the Atmospheric Sciences*, *51*(13), 1823-1842. doi: 10.1175/1520-0469(1994)051⟨1823:Tmapoe⟩2.0.Co;2
Mason, B. J. (1971). *The physics of clouds* [Book]. Oxford: Clarendon Press.
McFarquhar, G. M., Hsieh, T.-L., Freer, M., Mascio, J., & Jewett, B. F. (2015). The characterization of ice hydrometeor gamma size distributions as volumes in n0–lambda–mu phase space: Implications for microphysical process modeling [Journal Article]. *Journal of the Atmospheric Sciences*, *72*(2), 892-909. doi: 10.1175/jas-d-14-0011.1
Milbrandt, J. A., & Yau, M. K. (2005). A multimoment bulk microphysics parameterization. part i: Analysis of the role of the spectral shape parameter [Journal Article]. *Journal of the Atmospheric Sciences*, *62*(9), 3051-3064. doi: 10.1175/Jas3534.1
Morrison, H., & Gettelman, A. (2008). A new two-moment bulk stratiform cloud microphysics scheme in the community atmosphere model, version 3 (cam3). part i: Description and numerical tests [Journal Article]. *Journal of Climate*, *21*(15), 3642-3659. doi: 10.1175/2008jcli2105.1
Morrison, H., & Grabowski, W. W. (2008). A novel approach for representing ice microphysics in models: Description and tests using a kinematic framework [Journal Article]. *Journal of the Atmospheric Sciences*, *65*(5), 1528-1548. doi: 10.1175/2007jas2491.1
Morrison, H., & Milbrandt, J. A. (2015). Parameterization of cloud microphysics based on the prediction of bulk ice particle properties. part i: Scheme description and idealized tests [Journal Article]. *Journal of the Atmospheric Sciences*, *72*(1), 287-311. doi: 10.1175/Jas-D-14-0065.1
Nogherotto, R., Tompkins, A. M., Giuliani, G., Coppola, E., & Giorgi, F. (2016). Numerical framework and performance of the new multiple-phase cloud microphysics scheme in regcm4.5: precipitation, cloud microphysics, and cloud radiative effects [Journal Article]. *Geoscientific Model Development*, *9*(7), 2533-2547. doi: 10.5194/gmd-9-2533-2016
Patel, R. N., Yuter, S. E., Miller, M. A., Rhodes, S. R., Bain, L., & Peele, T. W. (2021). The diurnal cycle of winter season temperature errors in the operational global forecast system (gfs) [Journal Article]. *Geophysical Research Letters*, *48*(20), e2021GL095101. doi: 10.1029/2021gl095101
Pollard, R. T., Rhines, P. B., & Thompson, R. O. R. Y. (1973). The deepening of the wind-mixed layer [Journal Article]. *Geophysical Fluid Dynamics*, *3*(4), 381-404. doi: 10.1080/03091927208236105
Pruppacher, H. R., & Klett, J. D. (2010). *Microphysics of clouds and precipitation* (2nd ed.) [Book]. Springer Netherlands. doi: 10.1007/978-0-306-48100-0
Putman, W. M., & Lin, S. H. (2007). Finite-volume transport on various cubed-sphere grids [Journal Article]. *Journal of Computational Physics*, *227*(1), 55-78. doi: 10.1016/j.jcp.2007.07.022
Randles, C. A., Da Silva, A. M., Buchard, V., Colarco, P. R., Darmenov, A., Govindaraju, R., … Flynn, C. J. (2017). The merra-2 aerosol reanalysis, 1980 - onward, part i: System description and data assimilation evaluation [Journal Article]. *J Clim*, *30*(17), 6823-6850. doi: 10.1175/JCLI-D-16-0609.1

Rasch, P. J., & Kristjánsson, J. E. (1998). A comparison of the ccm3 model climate using diagnosed and predicted condensate parameterizations [Journal Article]. *Journal of Climate*, *11*(7), 1587-1614. doi: 10.1175/1520-0442(1998)011⟨1587:Acotcm⟩2.0.Co;2

Rienecker, M. M., Suarez, M. J., Gelaro, R., Todling, R., Bacmeister, J., Liu, E., ... Woollen, J. (2011). Merra: Nasa's modern-era retrospective analysis for research and applications [Journal Article]. *Journal of Climate*, *24*(14), 3624-3648. doi: 10.1175/Jcli-D-11-00015.1

Rotstayn, L. D. (1997). A physically based scheme for the treatment of stratiform clouds and precipitation in large-scale models. i: Description and evaluation of the microphysical processes [Journal Article]. *Quarterly Journal of the Royal Meteorological Society*, *123*(541), 1227-1282. doi: 10.1002/qj.49712354106

Seifert, A., & Beheng, K. D. (2005). A two-moment cloud microphysics parameterization for mixed-phase clouds. part 1: Model description [Journal Article]. *Meteorology and Atmospheric Physics*, *92*(1-2), 45-66. doi: 10.1007/s00703-005-0112-4

Stephens, G. L., Li, J. L., Wild, M., Clayson, C. A., Loeb, N., Kato, S., ... Andrews, T. (2012). An update on earth's energy balance in light of the latest global observations [Journal Article]. *Nature Geoscience*, *5*(10), 691-696. doi: 10.1038/Ngeo1580

Straka, J. M. (2009). *Cloud and precipitation microphysics* [Book]. Cambridge: Cambridge University Press. doi: 10.1017/cbo9780511581168

Swales, D. J., Pincus, R., & Bodas-Salcedo, A. (2018). The cloud feedback model intercomparison project observational simulator package: Version 2 [Journal Article]. *Geoscientific Model Development*, *11*(1), 77-81. doi: 10.5194/gmd-11-77-2018

Tiedtke, M. (1993). Representation of clouds in large-scale models [Journal Article]. *Monthly Weather Review*, *121*(11), 3040-3061. doi: 10.1175/1520-0493(1993)121⟨3040:Rocils⟩2.0.Co;2

Tong, M. J., Zhu, Y. Q., Zhou, L. J., Liu, E. M., Chen, M., Liu, Q. H., & Lin, S. A. J. (2020). Multiple hydrometeors all-sky microwave radiance assimilation in fv3gfs [Journal Article]. *Monthly Weather Review*, *148*(7), 2971-2995. doi: 10.1175/Mwr-D-19-0231.1

Trenberth, K. E., Fasullo, J. T., & Kiehl, J. (2009). Earth's global energy budget [Journal Article]. *Bulletin of the American Meteorological Society*, *90*(3), 311-323. doi: 10.1175/2008bams2634.1

Tripoli, G. J., & Cotton, W. R. (1980). A numerical investigation of several factors contributing to the observed variable intensity of deep convection over south florida [Journal Article]. *Journal of Applied Meteorology*, *19*(9), 1037-1063. doi: 10.1175/1520-0450(1980)019⟨1037:Aniosf⟩2.0.Co;2

Wild, M., Hakuba, M. Z., Folini, D., Dorig-Ott, P., Schar, C., Kato, S., & Long, C. N. (2019). The cloud-free global energy balance and inferred cloud radiative effects: an assessment based on direct observations and climate models [Journal Article]. *Clim Dyn*, *52*(7), 4787-4812. doi: 10.1007/s00382-018-4413-y

Wisner, C., Myers, C., & Orville, H. D. (1972). Numerical model of a hail-bearing cloud [Journal Article]. *Journal of the Atmospheric Sciences*, *29*(6), 1160-1181. doi: 10.1175/1520-0469(1972)029⟨1160:Anmoah⟩2.0.Co;2

Xu, K. M., & Randall, D. A. (1996). A semiempirical cloudiness parameterization for use in climate models [Journal Article]. *Journal of the Atmospheric Sciences*, *53*(21), 3084-3102. doi: 10.1175/1520-0469(1996)053⟨3084:Ascpfu⟩2.0.Co;2

Zhao, Q. Y., Black, T. L., & Baldwin, M. E. (1997). Implementation of the cloud prediction scheme in the eta model at ncep [Journal Article]. *Weather and Forecasting*, *12*(3), 697-712. doi: 10.1175/1520-0434(1997)012⟨0697:Iotcps⟩2.0.Co;2

Zhao, Q. Y., & Carr, F. H. (1997). A prognostic cloud scheme for operational nwp models [Journal Article]. *Monthly Weather Review*, *125*(8), 1931-1953. doi: 10.1175/1520-0493(1997)125⟨1931:Apcsfo⟩2.0.Co;2

Zhou, L. J., Bao, Q., Liu, Y. M., Wu, G. X., Wang, W. C., Wang, X. C., … Li, J. D. (2015). Global energy and water balance: Characteristics from finite-volume atmospheric model of the iap/lasg (famil1) [Journal Article]. *Journal of Advances in Modeling Earth Systems*, *7*(1), 1-20. doi: 10.1002/2014ms000349

Zhou, L. J., Lin, S. J., Chen, J. H., Harris, L. M., Chen, X., & Rees, S. L. (2019). Toward convective-scale prediction within the next generation global prediction system [Journal Article]. *Bulletin of the American Meteorological Society*, *100*(7), 1225-1243. doi: 10.1175/Bams-D-17-0246.1

Supporting Information for "Weather Prediction in SHiELD: Effect from GFDL Cloud Microphysics Scheme Upgrade"

Linjiong Zhou[1,2], Lucas Harris[2], Jan-Huey Chen[2,3], Kun Gao[1,2], Huan Guo[2],

Baoqiang Xiang[2,3], Mingjing Tong[2], James Huff[2,3], and Matthew Morin[2,3]

[1]Program in Atmospheric and Oceanic Sciences, Princeton University, Princeton, New Jersey, USA.

[2]National Oceanic and Atmospheric Administration / Geophysical Fluid Dynamics Laboratory, Princeton, New Jersey, USA.

[3]University Corporation for Atmospheric Research, Boulder, Colorado, USA.

Contents of this file

1. Figure S1. 10-day anomaly correlation coefficient (ACC) and bias evolution of (1st and 2nd columns) geopotential height (units: m), (3rd and 4th columns) temperature (units: K), and (5th and 6th columns) specific humidity (units: ($g\ kg^{-1}$)) at (from top row to bottom row) 100, 200, 250, 500, 700, 850, and 1000 hPa pressure levels. Blue line is OLD (original GFDL MP), orange line is CTRL (new GFDL MP).

2. Figure S2. 10-day averaged geographical distribution of the biases of (1st to 3rd columns) geopotential height (units: m), (4th to 6th columns) temperature (units: K), and (7th to 9th columns) specific humidity (units: $g\ kg^{-1}$) at (from top row to bottom row) 100, 200, 250, 500, 700, 850, and 1000 hPa pressure levels. For each variables, from the first to the third panels are OLD (original GFDL MP), CTRL (new GFDL MP), and

CTRL minus OLD. The numbers in the title of each panel are the bias and root mean square error.

3. Figure S3. Similar to Figure S1, but for (blue) CTRL, (orange) CPSD, (green) AERO, and (red) CPSD_AERO.

Introduction This supporting document includes additional figures to support the weather prediction evaluation in the main paper.

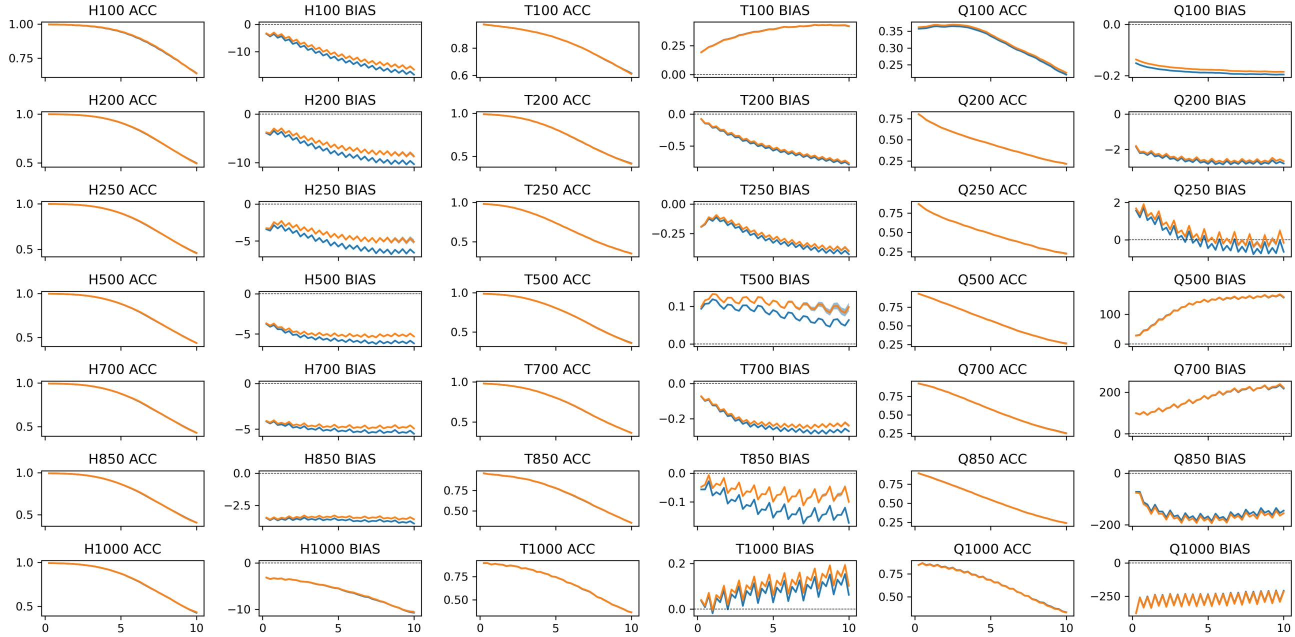

Figure S1. 10-day anomaly correlation coefficient (ACC) and bias evolution of (1st and 2nd columns) geopotential height (units: m), (3rd and 4th columns) temperature (units: K), and (5th and 6th columns) specific humidity (units: $g\ kg^{-1}$) at (from top row to bottom row) 100, 200, 250, 500, 700, 850, and 1000 hPa pressure levels. Blue line is OLD (original GFDL MP), orange line is CTRL (new GFDL MP).

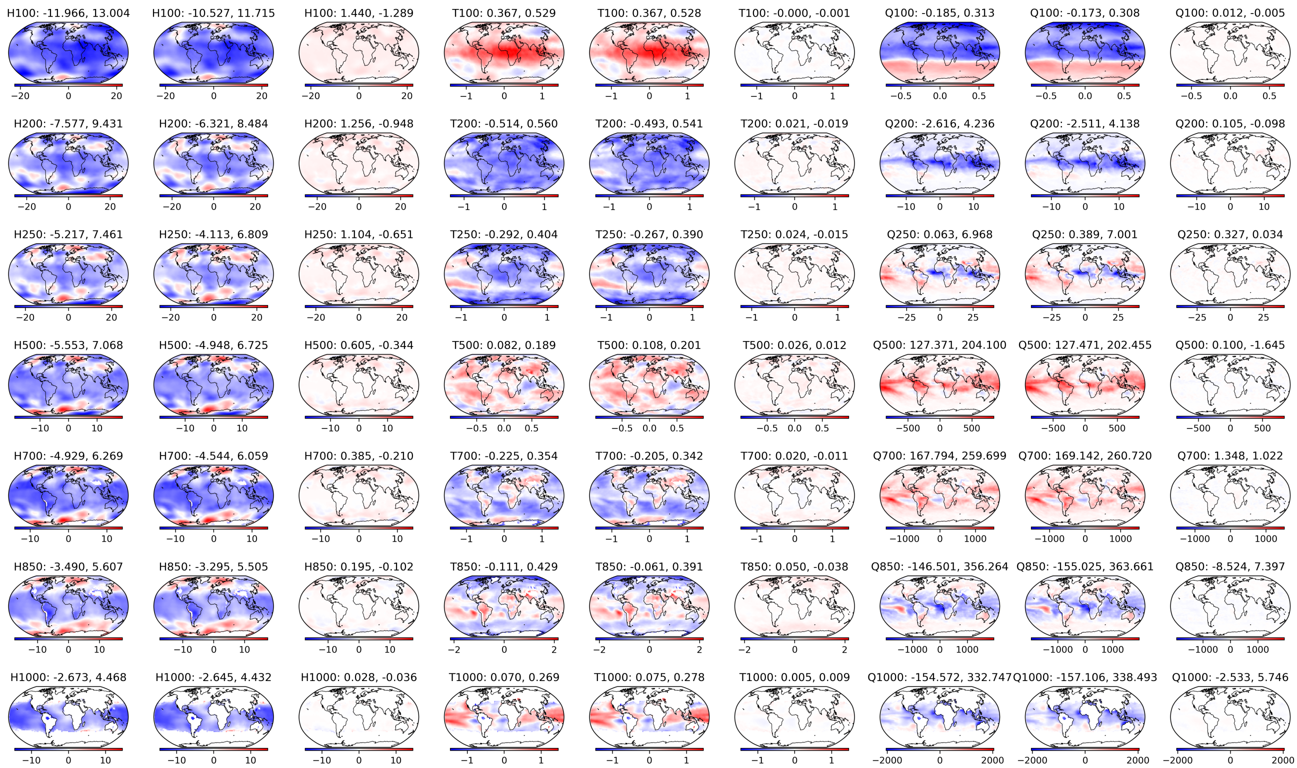

Figure S2. 10-day averaged geographical distribution of the biases of (1st to 3rd columns) geopotential height (units: m), (4th to 6th columns) temperature (units: K), and (7th to 9th columns) specific humidity (units: $g\ kg^{-1}$) at (from top row to bottom row) 100, 200, 250, 500, 700, 850, and 1000 hPa pressure levels. For each variables, from the first to the third panels are OLD (original GFDL MP), CTRL (new GFDL MP), and CTRL minus OLD. The numbers in the title of each panel are the bias and root mean square error.

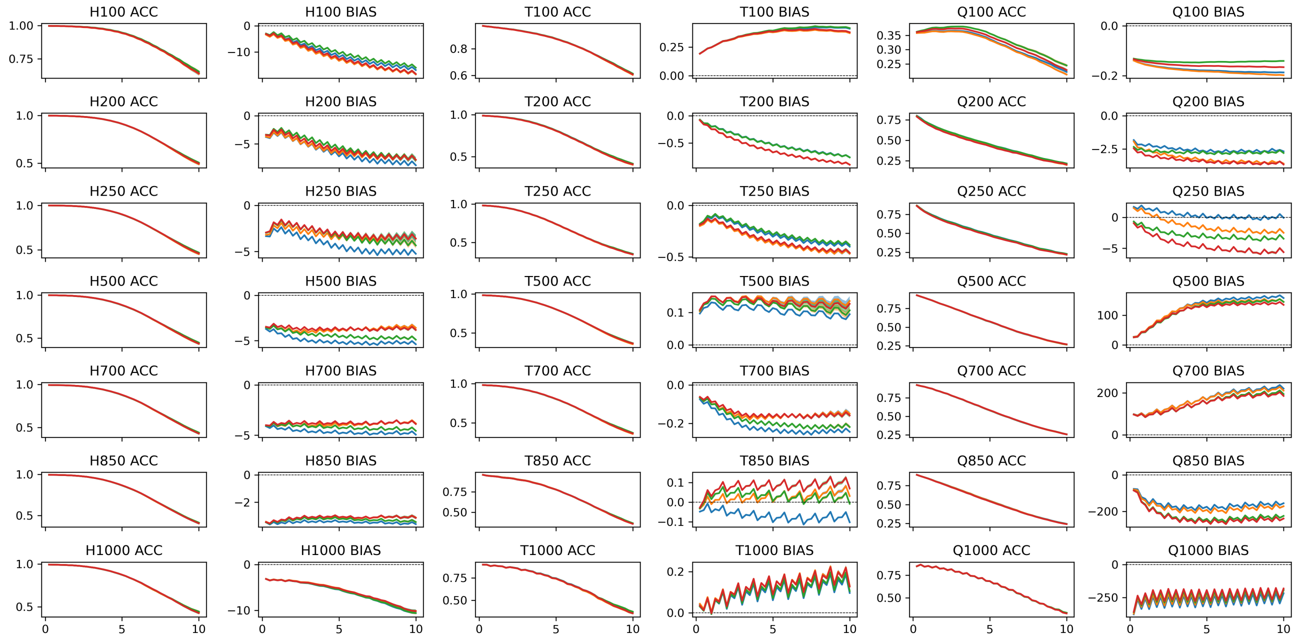

Figure S3. Similar to Figure S1, but for (blue) CTRL, (orange) CPSD, (green) AERO, and (red) CPSD_AERO.